Word Count: 12389

Revision 1

Heterogeneous and retarded phase transformation of ferrihydrite on montmorillonite surface: the important role of surface interactions

Hongyan Wei [1,2,3], Jing Liu [4], Qingze Chen [1, 2, 3], Runliang Zhu [1, 2, 3]*, Lixia Yan [5], Yixuan Yang [1, 2, 3], Xiaoliang Liang [1, 2, 3], Jianxi Zhu [1, 2, 3], Hongping He [1, 2, 3]

1. CAS Key Laboratory of Mineralogy and Metallogeny/Guangdong provincial Key Laboratory of Mineral Physics and Materials, Guangzhou Institute of Geochemistry, Chinese Academy of Sciences (CAS), Guangzhou, 510640 China

2. CAS Center for Excellence in Deep Earth Science, Guangzhou 510640, China

3. University of Chinese Academy of Science, Beijing, 100049 China

4. State Key Laboratory of Lunar and Planetary Sciences, Macau University of Science and Technology, Taipa 999078, Macau, China

5. School of Geographical Sciences, Shanxi Normal University, Taiyuan, 030031, China

*Corresponding author. Tel: 86-020-85297603

E-mail: zhurl@gig.ac.cn

ABSTRACT

The formation of heteroaggregates is critical to dictating the stabilization and transformation of nanominerals and mineral nanoparticles (NMMNs) in the nature, but the underlying mechanisms remain to be deciphered. In this work, we study the effect of surface interactions between ferrihydrite (Fh) and montmorillonite (Mnt) within their heteroaggregates on the transformation behaviors of Fh. A series of heteroaggregates composing of Fh and Mnt were synthesized by modulating their mass ratios and synthesis methods, i.e., directly complexing Fh with Mnt (Fh-Mnt) or in-situ growing Fh on Mnt (Fh/Mnt). The structural characterization results from XRD, TG-DSC, TEM, and FTIR indicated that Fh particles coated more evenly on the Mnt surface within the heteroaggregates synthesized by in-situ growing Fh on Mnt and with lower Fh to Mnt ratio, and accordingly these heteroaggregates showed stronger surface interactions between Fh and Mnt. The phase transformation of Fh to hematite (Hem) on the heteroaggregates can be significantly affected during the heating treatment. Compared with that of pure Fh, the transformation of Fh on all of the heteroaggregates was retarded (e.g., slower transformation rate and smaller produced Hem particles), particularly for the samples with stronger surface interactions (e.g., Fh/Mnt with lower Fh to Mnt ratio). Noticeably, the heated heteroaggregates may simultaneously contain pristine Fh, intermediate maghemite, and transformed Hem, showing a heterogeneous transformation behavior of Fh. The strong interactions between Fh and Mnt will benefit the dispersion of Fh and restrict the structural rearrangement of Fh (particularly those at the interface) during the phase transformation process, resulting in retarded and heterogenous transformation of Fh on these heteroaggregates. The findings of this work not only enrich our knowledge of the phase transformation characteristics of Fh but also

43 advance our understanding of the important role of mineral surface interactions on
44 stabilizing NMMNs in the nature.
45
46 **Keywords**: nanominerals and mineral nanoparticles; ferrihydrite; clay minerals;
47 surface interactions; phase transformation
48

INTRODUCTION

Almost all geochemical processes in the nature start from the mineral surfaces (Putnis 2014; Liu et al. 2021a; Zhu et al. 2021). The omnipresent nanominerals and mineral nanoparticles (NMMNs) in the supergene environment always have small particle sizes and large specific surface areas, and thus contribute the major mineral surfaces for a diversity of surface reactions, e.g., adsorption/desorption, catalytic synthesis/degradation, and crystallization/dissolution (Banfield and Zhang 2001; Hochella et al. 2008, 2019). On the other hand, the large surface energy of NMMNs also makes them rather fragile to dissolution, growth, and/or phase transformation (i.e., with metastable structures) (Navrotsky et al. 2008, 2010). As such, in addition to the structural characteristics and surface reactivities, the generation and stabilization of NMMNs in the nature are drawing significant concerns as well (He et al. 2021; Yan et al. 2021).

One well-studied NMMNs is ferrihydrite (Fh), the first formed iron (oxyhydr)oxide mineral phase during the hydrolysis of Fe^{3+} (Hochella et al. 2005; Michel et al. 2007a, b). On the one hand, Fh has been regarded as an important geosorbent (Hassellov and von der Kammer 2008; Liu et al. 2018, 2021b) and natural catalyst (Xu et al. 2017; Zhu et al. 2022) participating in a variety of geological and geochemical processes; on the other hand, Fh can easily transform to more stable iron (oxyhydr)oxides, e.g., to goethite (Gth) through dissolution-recrystallization and to hematite (Hem) through dehydration, which subsequently dictates the cycling and bioavailability of Fe, and the overall composition and reactivity of iron (oxyhydr)oxides in the nature (Raiswell and Canfield 2012; Yan et al. 2020). As such, clarifying the phase transformation processes of Fh and the underlying

71 mechanisms is of high importance and has been a subject of extensive studies (Francisco
72 et al. 2016; Yan et al. 2020, 2021; Sheng et al. 2020, 2021).

73 Numerous studies have shown that various environmental factors (e.g., pH,
74 temperature, humidity, concurrent chemicals) can affect the phase transformation of Fh and
75 the final products (Loan et al. 2005; Das et al. 2011a, b; Yang et al. 2021). For example,
76 the concurrent ions/molecules, by affecting the aggregation, dissolution, and/or
77 dehydration of Fh, may inhibit (Das et al. 2011a; Francisco et al. 2018) or accelerate (Yee
78 et al. 2006; Li et al. 2020) the transformation rate of Fh. Interestingly, other concurrent
79 NMMNs in the nature may be complex with Fh, and the resulting heteroaggregates can
80 affect the phase transformation of Fh as well (Yan et al. 2020, 2021). For instance, Fh is
81 often complex with clay minerals to form heteroaggregates in the nature, as the negatively
82 charged large surface of clay minerals can effectively immobilize Fe^{3+} and its hydrolyzed
83 species, benefiting the formation of Fh on clay minerals (Dimirkou et al. 2002; Zeng et al.
84 2020). Several studies carried out in aqueous environments showed that clay minerals can
85 inhibit the transformation of Fh, which has been mainly attributed to the inhibition effects
86 of dissolved ions (e.g., silicate, Al^{3+}) from clay minerals (Schwertmann 1979, 1988;
87 Schwertmann et al. 2000). However, the effects of surface interactions between clay
88 minerals and Fh, which have contributed largely to the formation of their heteroaggregates,
89 on the stabilization of Fh in the nature and the underlying mechanisms remain largely
90 unknown.

91 Most previous studies involving Fh transformation with different concurrent materials
92 have been conducted in aqueous environments (Yee et al. 2006; Das et al. 2011a; Li et al.
93 2020), while the transformation of Fh under nonaqueous environments has been much less

94 studied, despite its widespread occurrence in the nature. One such situation is the
95 transformation under high temperature during the input of intensive energy, which can be
96 caused by wildfire (Gibson et al. 2018), agricultural and industrial activities (Liu et al.
97 2008), volcano eruption (Girona et al. 2021), etc. Indeed, the earth is intrinsically
98 flammable, which results in the widespread wildfires (Bowman et al. 2009; Tang et al.
99 2020). Previous studies demonstrated that the average burned areas by wildfires were 463
100 million hectares/year during 2001-2018 (Lizundia-Loiola et al. 2020) and the temperature
101 of soil surface can reach up to 850°C (Certini 2005). Moreover, an apparent increase in
102 wildfire has been found worldwide due to climate change and human activity. For example,
103 about 79,000 wildfires were recorded worldwide in August 2019 compared to just 16,000
104 wildfires in August 2018 (Shi and Touge 2022). The model simulations demonstrated that
105 the wildfire days in California will increase from 36 days/year during 1970-1999 to 71
106 days/year by 2070-2099 (Dong et al. 2022). In addition, previous studies showed that the
107 mineralogical properties of soils could be affected by wildfire (Yusiharni and Gilkes 2012;
108 Terzano et al. 2021). As such, studying the transformation processes of Fh in the
109 heteroaggregates (of Fh and clay minerals) at high temperature and the underlying
110 mechanisms is highly necessary in that 1) the heteroaggregates are widespread on Earth's
111 surface; 2) the surface interactions between Fh and clay minerals will make the
112 transformation process rather complex, which, however, have been overlooked in previous
113 studies; 3) it is an ideal condition for clarifying how mineral surface interactions can affect
114 the stability and transformation of NMMNs (as the effects of dissolved ions from clay
115 minerals can be excluded); 4) high temperature resulted from wildfire is widespread in the
116 nature.

This study aims to unveil the influence of surface interactions between clay minerals and Fh on the transformation of Fh during heat treatment. Two different types of heteroaggregates composing of Fh and montmorillonite (Mnt) are synthesized, i.e., directly complexing Fh with Mnt (Fh-Mnt) and in-situ growing of Fh on Mnt (Fh/Mnt). We expect these heteroaggregates will have different surface interaction behaviors and thus provide proper samples for the study. Heating treatment (300-600°C) will be applied to accelerate the transformation process, and simulate the temperature conditions for wildfire. We are concerned with how Mnt can affect the transformation rate and pathway of Fh, and the mineral phases and morphology of the samples before and after heating will be studied in detail.

METHODS

Synthesis of Fh and the mineral heteroaggregates

The synthesis of Fh was based on the protocol of Cornell and Schwertmann (2003). In brief, $Fe(NO_3)_3 \cdot 9H_2O$ and NaOH were titrated to pH 7.5 under continuous magnetic stirring. Subsequently, the suspension was allowed to equilibrate for a period of approximately 2 h. All precipitates were washed three times with ultrapure water by centrifugation and then freeze-dried, ground, and saved in a desiccator. Two different types of heteroaggregates were synthesized in this work. The first one is obtained by complexing pre-synthesized Fh with Mnt (Fh-Mnt), and the second one is obtained by in-situ growing Fh on Mnt (Fh/Mnt). The specific methods for the synthesis of the heteroaggregates can be found in supplementary materials (Text. S1). The resulting samples are named as Fha-Mntb or Fha/Mntb (e.g., Fh2-Mnt1 or Fh2/Mnt1 represent the mass ratio of Fh to Mnt being 2:1).

Thermal treatment of the samples

Thermal treatment of the samples was conducted in air. Typically, these samples were placed in

corundum crucibles and then heated at selected temperatures (300, 400, or 600°C) for different time intervals (0.5, 1, 2, 4, 6, or 8 h), and then naturally cooled to room temperature. The thermally treated samples were denoted as Fha-Mntb-temperature-time or Fha/Mntb -temperature-time, e.g., Fh2-Mnt1-400-4 represents the sample of Fh2-Mnt1 being heated at 400°C for 4 h. The heating temperatures were selected based on the temperatures that could occur in the surface soils during wildfire and were beneficial to observing the dry-heating transformation of Fh. The heating times were selected to better investigate the transformation of Fh under the influence of Mnt.

Characterization methods

Structure analysis of the samples was performed by X-ray powder diffraction (XRD, Bruker D8 ADVANCE) and Fourier transform infrared spectroscopy (FTIR, PerkinElmer). XRD was used to determine the mineral phases of the final products. In addition, we also used in-situ XRD to record the samples in real-time during the heating process. See the supplementary materials for specific operation methods. The morphology of the obtained samples was characterized by scanning electron microscopy (SEM, Carl Zeiss Supra 55) and transmission electron microscopy (TEM, FEI Talos F200S), and energy diffraction spectrum (EDS) and selected area electron diffraction (SAED) analysis were performed with an FEI Talos F200S TEM at an accelerating voltage of 200 kV. Thermogravimetric (TG) analysis with differential scanning calorimetry (DSC) was performed on a Netzsch STA 449F3 instrument. The magnetic susceptibility (χ) of different heated samples at room temperature was determined in the magnetic field of 200 A m^{-1} using a Kappabridge MFK2 instrument at an operating frequency of 976 Hz. The magnetic susceptibilities of pure Fh before and after heating were quality-normalized to compare with the mass of Fh in the heteroaggregates. Moreover, the degree of the transformation of Fh in different samples was decided by the selective dissolution experiments, in which the Fh can be dissolved by 0.2 M ammonium oxalate, and crystalline iron oxide can be dissolved by 6 M HCl. The specific operation steps and parameters for these characterization methods can be found in supplementary materials (Text. S2).

RESULTS

The structural characteristics of the samples before heating

The transformation of Fh in the heteroaggregates should closely relate to the interaction between Fh and Mnt, which we propose would relate to the synthesis methods and the mass ratio between Fh and Mnt. In this term, the structural characteristics of the synthesized samples before heating were investigated. According to the XRD results, Fh possesses two broad reflections at 2θ = 36° and 63° (Fig. 1a), well matching with the standard pattern of 2-line Fh (Michel et al. 2007a); Mnt is rich in Na^+ with the d_{001}-value of 1.28 nm, and contains a small amount of quartz (Qz) impurities (Fig. 1a). For Fh-Mnt, the intensity of the Mnt 001 reflection decreased with increasing Fh content (Fig. 1b), which should be attributed to the irregular stacking of Mnt layers caused by complexing with Fh during the drying process (Celis et al. 1998), and negligible shifting of the 001 reflections of Mnt suggested little Fh in the interlayer of Mnt. Similar results were obtained for Fh/Mnt, except that the 001 reflection of Mnt becomes rather weak or even undetectable at high Fh content (Fig. 1c). According to previous studies of the iron polycations modified Mnt, the formation of a "house-of-card" structure can destroy the orderly stacking of Mnt layers, leading to the disappearance of 001 reflections (Yuan et al. 2008). It is difficult to identify the Fh phase on the heteroaggregates by XRD due to its weak characteristic reflections, but the TEM results hereinafter will prove the presence of Fh on these heteroaggregates.

SEM and TEM images together unveiled the morphology of the samples (Fig. 1d-k). Fh aggregates were composed of spherical nanoparticles with diameters of 3-5 nm (Fig. 1d and h, Fig. S1a). The SAED result showed two diffuse diffraction rings at d = 0.25 and

188 0.15 nm (the inset in Fig. 1h), indicating the typical structure of 2-line Fh (Michel et al.
189 2007a). The initial Mnt demonstrated a lamellar structure with randomly distributed pores
190 (Fig. S1b). For the Fh-Mnt, Fh aggregates were shown to disperse on the surfaces of Mnt
191 lamellas (Fig. 1e-f and i-j), and Fh aggregates become smaller in size with decreasing Fh
192 content (Fig. 1f and j). As for Fh/Mnt, two diffraction rings at 0.25 and 0.15 nm in the
193 SAED image verified the presence of Fh (the inset of Fig. 1k). Unlike the situation of Fh-
194 Mnt, it was difficult to recognize the segregation of Fh aggregates and Mnt lamellas on
195 Fh/Mnt, indicating that Fh is quite uniformly dispersed on the Mnt surface (Fig. 1g and k).
196 The EDS mapping results showed that the distribution of Fe on Fh-Mnt was quite uneven,
197 with the content ranging from 15% to 97% in different selected areas (Fig. S2); however,
198 Fe dispersed more evenly on Fh/Mnt, with its relative content in the range of 37%~68% in
199 different selected areas (Fig. S3).

200 The interaction between Fh and Mnt on different heteroaggregates was also
201 investigated by FTIR spectra (Fig. S4, Table. S2). The shift of Al-OH vibration bands on
202 Mnt (3623 and 913 cm^{-1}) (Fig. S4a) indicated that the polarity of O-H in Al-OH decreased,
203 which can be ascribed to the formation of hydrogen bonds and Al-O-Fe bonds between Fh
204 and Mnt. Similar results were reported for the heteroaggregates formed by iron
205 (oxyhydr)oxides and clay minerals in previous studies (Pokrovski et al. 2003; Wei et al.
206 2012; Shu et al. 2019). The absorption bands of adsorbed H_2O on Mnt (3426 and 1638 cm^{-1})
207 were shifted toward lower frequency for the heteroaggregates, which can be attributed
208 to the formation of hydrogen bonds between the water molecules on Mnt and the surface
209 groups (Fe-OH) on Fh (Dimirkou et al. 2002). The absorption band at 1082 cm^{-1} becomes
210 more obvious for the heteroaggregates (especially in the Fh2/Mnt1), which should be

211 ascribed to the formation of Si-O-Fe bonds (Ye et al. 2016). The locations of overlapping
212 bands (750-1300 cm^{-1}) were determined according to the second derivative spectra (Fig.
213 S4b), and the four components at 1112, 1084, 1036, and 1003 cm^{-1}, which were assigned
214 to the complex Si-O vibration bands (Pentrak et al. 2018), were slightly shifted on the
215 heteroaggregates. It should be noted that these changes in FTIR spectra for the
216 heteroaggregates were more obvious in Fh2/Mnt1 than those in Fh2-Mnt1, suggesting
217 stronger surface interactions in Fh2/Mnt1.
218 The TG curves showed that the residual weights of Fh, Fh2-Mnt1, Fh2/Mnt1, and Mnt
219 (after heating to 1200°C) remained at 90.9%, 85.2%, 81.0%, and 83.5%, respectively (Fig.
220 2a), and the weight loss for the samples should be ascribed to dehydration and
221 dehydroxylation. According to the composition of Fh and Mnt in the heteroaggregates and
222 the TG curves of pure Fh and Mnt, we calculated the theoretical TG curves of the Fh and
223 Mnt mixture with a mass ratio of 2:1 (Fh2+Mnt1), and the residual weight should be 88.4%,
224 evidently higher than that of both Fh2-Mnt1 and Fh2/Mnt1. This discrepancy indicated
225 more H_2O and/or OH in the two heteroaggregates, which suggested that Mnt can affect the
226 microstructure of Fh aggregates and/or the crystallinity of Fh. Generally, the weight loss
227 below 200°C and between 200-700°C can be assigned to the loss of adsorbed water and
228 structural water/hydroxyl, respectively (Guggenheim and van Groos 2001; Khaorapapong
229 et al. 2010; Wang and Liu 2013). The theoretical weight losses below 200°C and between
230 200-700°C for the Fh and Mnt mixture were 7.5% and 4.0%, respectively. In this term, the
231 Fh2+Mnt1 mixture has less adsorbed water than both Fh2-Mnt1 (10.3%) and Fh2/Mnt1
232 (12.8%) (Fig. 2a); while its structural water/hydroxyl is the same as that of Fh2-Mnt1 (4.0%)
233 and less than that of Fh2/Mnt1 (5.6%), which suggested the weak crystallinity of in-situ

234 formed Fh on Fh2/Mnt1. Wei et al (2012) also reported more structural hydroxyls and
235 weaker crystallinity of Gth on the heteroaggregates of Gth and Kaolinite. The DSC curves
236 of Fh showed an exothermic peak at approximately 473°C, which could be assigned to the
237 formation of Hem (Rzepa et al. 2016; Pieczara et al. 2020). This exothermic peak increased
238 to 517°C for Fh2-Mnt1 and 561°C for Fh2/Mnt1, which indicated that the presence of Mnt
239 increased the transformation temperature of Fh, particularly for Fh/Mnt (Fig. 2b). These
240 results demonstrated that Mnt can affect the crystallization of Fh during its in-situ
241 formation process and increase the formation temperature of Hem, which again suggested
242 strong surface interactions between Fh and Mnt.

243 Above results from different characterization methods well demonstrated that by
244 changing the Fh and Mnt ratios and applying various synthesis methods, we can obtain the
245 heteroaggregates with different structures and surface interactions. In general, Fh/Mnt
246 showed more uniform dispersion of Fh on Mnt and better surface interactions between
247 these two components, as compared with Fh-Mnt. Besides, increasing Mnt content in the
248 heteroaggregates will benefit Fh dispersion on Mnt and result in better surface contact as
249 well. As such, the synthesized heteroaggregates will provide ideal samples for studying the
250 effects of mineral surface interactions on the phase transformation of Fh.

251 **Structural characteristics of the heated samples**

252 **The transformation rate of Fh and the transformed products.** The mineral phases
253 of heated Fh and Mnt were first characterized by XRD (Fig 3 and Fig S5). The
254 characteristic reflections of Hem in the heated Fh samples became observable only after
255 the heating temperature reached 270°C (4 h) (Fig. S5a). With increasing heating

temperature, the intensity of the reflections increased while the full width at half maximum (FWHM) of the reflections decreased (Fig. S5a and Table. S3), which suggested that more Fh transformed to Hem, with its crystallinity and particle size increasing as well. For the samples heated at 400°C, the calculated mean particle size (using the Scherrer equation) increased with rising heating duration: Fh-400-1 (14.5 nm) < Fh-400-2 (20.2 nm) < Fh-400-4 (22.7 nm) (Text. S3, Table. S4). As for the heated Mnt samples, their XRD patterns were almost the same, except for the sample heated at 600°C for 1 h, which showed a collapse of interlayer space (with a basal spacing of 0.96 nm) (Fig. S5b).

As for Fh-Mnt, we first studied the structure of the heated samples (400°C, 4 h) with different Mnt contents. The XRD results showed that the characteristic reflections of Hem became less evident with an increment of Mnt content, and the characteristic reflections almost became undetectable for Fh1-Mnt2-400-4 (Fig. 3a). The calculated particle size of Hem (using the Scherrer equation) also demonstrated that Hem particles were larger in Fh2-Mnt1-400-4 (19.1 nm) than in Fh1-Mnt1-400-4 (13.3 nm), but both were smaller than that in Fh-400-4 (22.7 nm) (Table. S4). Then, the effects of heating temperature and duration on the phase transformation of Fh2-Mnt1 were further investigated (Fig. 3b and c). Similar to the transformation of pure Fh, increasing heating temperature (from 300°C to 600°C) and duration (from 1 to 4 h) was beneficial to the transformation of Fh to Hem. Specifically, the characteristic reflections of Hem started to appear in the sample being heated at 400°C for 1 h (i.e., Fh2-Mnt1-400-1). Then, the reflection intensity increased and the FWHM decreased with the increment of heating temperature and duration, indicating

277 better crystallinity of the obtained Hem.

278 For Fh/Mnt, the obtained results were similar to those of Fh-Mnt, and the inhibition
279 effect of Mnt on the transformation of Fh was also related to Mnt content and the heating
280 temperature and duration (Fig. 3a-c). However, Mnt in Fh/Mnt showed an even stronger
281 inhibiting effect on the transformation of Fh than that in Fh-Mnt did (Fig. 3a-c). For
282 example, the characteristic reflections of Hem only appeared on the heteroaggregates with
283 the highest Fh content (Fh2/Mnt1), when all of the Fh/Mnt samples were heated at 400°C
284 for 4 h (Fig. 3a). Even for Fh2/Mnt1, no characteristics reflections of Hem can be detected
285 when the heating duration decreased to 1 h unless the temperature is increased to 600°C
286 (Fig. 3b and c).

287 In-situ XRD was further applied to detect the real-time structural changes of the
288 samples during the heating processes (Text. S4). First, the samples were heated at 450°C
289 and XRD patterns were obtained at different time intervals. The characteristic reflections
290 of Hem for pure Fh and Fh2-Mnt1 appeared after 0.5 h (Fig. S6a and b), which, however,
291 could not be observed for Fh1-Mnt1 even after heating for 3 h (Fig. S6c). As for Fh2/Mnt1,
292 only weak characteristic reflections of Hem could be observed after in-situ heating (Fig.
293 S6d). Then, the in-situ XRD patterns of the samples heated from 30 to 800°C were recorded,
294 and the results revealed that the transformation temperature of Fh in various samples
295 decreased in the order: Fh2/Mnt1 (650°C) > Fh2-Mnt1 (600°C) > Fh (500°C) (Fig. S7),
296 consistent with the results from DSC characterization (Fh2/Mnt1 (561°C) > Fh2-Mnt1
297 (517°C) > Fh (473°C)). The difference in transformation temperature of the two
298 characterization systems should result from the different heating rates and characterization

299 instruments.

300 Ammonium oxalate dissolution experiments were used to analyze the transformation
301 degree of Fh, and the Fe_o/Fe_t (the ratio of oxalate dissolved iron to total iron) value
302 represents the relative content of residual Fh in the heated products. The transformation of
303 pure Fh was nearly complete after heating at 400°C for 1, 2, and 4 h (with the residual Fh
304 below 5%) (Fig. 3d). As for Fh-Mnt, the residual Fh content decreased with the increment
305 of heating duration and Fh content. For example, the residual Fh content in Fh2-Mnt1-400-
306 4 was ~7%, whereas it was ~37% in Fh2-Mnt1-400-1 and ~50% in Fh1-Mnt1-400-4. With
307 respect to Fh/Mnt, the residual Fh content was >90% even after heating at 400°C for 4 h
308 for all of the three heteroaggregates with different Fh content, which indicated a much
309 lower transformation rate of Fh, as compared with Fh and counterpart Fh-Mnt samples
310 heated under the same conditions. These results were well in agreement with those from
311 XRD characterization, and in combination they showed the different transformation rates
312 of Fh in these heteroaggregates, suggesting the significant effects of surface interactions
313 between Fh and Mnt on the transformation process.

314 **Magnetic evolution of the samples during the transformation process.** Previous
315 studies have shown that the dry-heating transformation of Fh in the presence of other
316 concurrent chemicals (e.g., silicate, phosphate) could experience an intermediate process
317 where Mgh occurs, resulting in magnetic enhancement (Rzepa et al. 2016; Pieczara et al.
318 2020). To reveal the magnetism change, and thus the mineral phase evolution, of the
319 samples during treatment, the magnetic susceptibility (χ) of different heated samples was

measured, and the obtained value was plotted as a function of the heating time at 400°C (Fig. 4). Fh was paramagnetic at room temperature with a χ value of 3.1 $\times 10^{-6}$ m^3 kg^{-1}, consistent with the results of previous studies (Rzepa et al. 2016; Jiang et al. 2018). Heating treatment significantly decreased the χ of Fh, which reached ~2.0 $\times 10^{-7}$ m^3 kg^{-1} after 1 h of treatment and then remained relatively constant. A similar lowering of χ was reported by Rzepa et al. (2016) and Cabello et al. (2009). The χ of Mnt was 1.1 $\times$ 10^{-7} m^3 kg^{-1}, and nearly unchanged during the heating process, suggesting that no secondary magnetic minerals were formed.

On the other hand, the χ value of Fh2-Mnt1 increased from 2.5 $\times$ 10^{-6} to 3.7 $\times$ 10^{-6} m^3 kg^{-1} after the sample being heated at 400°C for 2 h. Then, further rising the heating duration led to a decrease of χ value (to 2.4 $\times 10^{-6}$ m^3 kg^{-1} after 8 h). The first increase of χ might be attributed to the formation of Mgh (will be proved by HRTEM), while the further decrease of χ should be accounted for the transformation of Mgh to Hem (Jiang et al. 2018). As for Fh2/Mnt1, the evident rise of χ value was also observed during the first 1 h heating stage, and then it further increased gradually to 3.7 $\times$ 10^{-6} m^3 kg^{-1} as the heating duration reached 8 h (i.e., the χ value being doubled). These results also suggested the formation of Mgh during the heating of Fh2/Mnt1, while the further transformation of Mgh to Hem was slowed down by Mnt, as compared with the situation of Fh2-Mnt1.

Overall, the obtained results from magnetic characterization provided additional evidence showing the different phase transformation behaviors of Fh in pure Fh, Fh2-Mnt1, and Fh2/Mnt1. However, we should also note that the XRD results did not detect the

341 presence of Mgh (Fig. 3 and Fig. S7) during the heating treatment of the samples, which
342 suggested that the content of Mgh in these samples should be very small and below the
343 detection limit by XRD. The following TEM results, however, did detect the existence of
344 Mgh (see Fig. 6 and 7).

345 **The morphology and microstructure of the products.** Above characterization
346 results of the heated samples only gave the average information of the sample, while these
347 heteroaggregates, composed of two mineral components with strong surface interactions,
348 indeed can be structurally quite heterogeneous at the micro-nanoscale (as shown by Fig.
349 1). As such, SEM and TEM were applied to investigate the morphology and microstructure
350 of the heated samples. For pure Fh heated at 400°C for 4 h (i.e., Fh-400-4), a quasi-
351 spherical morphology was observed for the samples in the SEM and TEM images (Fig. 5a
352 and b). The HRTEM image showing a lattice fringe of 0.37 nm (012 plane) verified that
353 these nanoparticles were Hem (Fig. 5c), consistent with the XRD results. The size
354 distribution of the heated product, which was measured statistically using the TEM image,
355 showed an average particle size of 27.4 ± 6.9 nm (the inset in Fig. 5b).
356 As for the heated Fh-Mnt (400°C, 4 h), the obtained Hem also demonstrated a quasi-
357 spherical morphology (Fig. 5d-i), and the average particle sizes in Fh2-Mnt1-400-4 and
358 Fh1-Mnt1-400-4 were 17.5 ± 3.1 (the inset in Fig. 5e) and 7.5 ± 1.3 nm (the inset in Fig.
359 5h), respectively, evidently smaller than that in Fh-400-4 (27.4 ± 6.9 nm). Clearly,
360 increasing Mnt content in the heteroaggregates will result in smaller particle sizes in the
361 heated products. The individual particles were identified by different colors in the HRTEM

362 images (Fig. 5f and i). The detected interplanar spacings of 0.27 and 0.18 nm for the
363 particles, which correspond to the (104) and (024) planes of Hem, respectively (Fig. 5f and
364 i), demonstrated that these particles were primarily Hem as consistent with the results of
365 XRD.

366 Moreover, the HRTEM images of Fh2-Mnt1-400-4 were further analyzed with the
367 fast Fourier transform (FFT) pattern and the masking tool on the FEI TIA software (Tecnai
368 Imaging & Analysis). The particles were stacked in the detected area and showed good
369 crystallinity with clear lattice fringes (Fig. 6a). The FFT patterns of areas "b" and "c" in
370 Fig. 6a showed that the Hem particles were along the $[\bar{2}2\bar{1}]$ and $[4\bar{4}\bar{1}]$ directions (Fig. 6b
371 and c), respectively. The FFT pattern of area "d" in Fig 6a gave four sets of diffraction
372 patterns belonging to Mgh and Hem (Fig. 6d). Then, the diffraction patterns with the spots
373 related to the Hem and other Mgh particles were excluded by the mask except in the $[\bar{1}2\bar{2}]$
374 direction of Mgh (Fig. 6e), and the corresponding inverse fast Fourier transform (IFFT)
375 image (Fig. 6f) showed a single particle with interplanar spacings of 0.59 and 0.37 nm,
376 belonging to the Mgh (011) and (210) planes, respectively. The angle between two adjacent
377 facets was 71.5°, consistent with the theoretical value of 71.6°. Moreover, Mgh particles
378 were also identified by FFT pattern analysis (Fig. 6g-j), which showed that Mgh particles
379 were along the $[02\bar{2}]$ (Fig. 6i) and $[\bar{1}11]$ directions (Fig. 6j). The single Mgh particle was
380 identified with dotted lines in the HRTEM images (Fig. 6g and i). The above results showed
381 that although the heated products were mainly Hem (as confirmed by XRD results), some
382 small Mgh particles could also be found in the HRTEM patterns, which suggested that the
383 microstructure of the heteroaggregate after heating was heterogeneous. This heterogeneous

384 phase transformation of Fh might be related to the different effects of the surface
385 interactions between Fh and Mnt (will be further discussed hereinafter).

386 With respect to the heated Fh/Mnt, Fh2/Mnt1-400-4 (i.e., heated at 400°C for 4 h) did
387 not present obvious nanoparticles in the SEM and TEM images (Fig 5j and k), and two
388 diffraction rings with d = 0.25 and 0.15 nm in the SAED pattern confirmed a large amount
389 of residual Fh (the inset in Fig. 5k). Besides, the HRTEM image hardly showed any lattice
390 fringes (Fig. 5l), which further verified the weak transformation of Fh, consistent with the
391 XRD results (Fig. 3a). However, crystalline particles could still be observed in the HRTEM
392 images obtained from other areas of this sample (Fig. 7a). In specific, the FFT pattern of
393 selected areas ("b" and "c") from Fig 7a showed the (200) plane of Mnt (Fig. 7b and c),
394 which indeed can be observed in the whole area of Fig. 7a. The FFT pattern of another
395 selected area "d" showed two sets of diffraction patterns belonging to Mnt and Mgh (Fig.
396 7d and e), in which Mgh was along the [1$\bar{6}$9] direction according to the FFT analysis. The
397 FFT pattern (Fig. 7f) with the Mnt spots was excluded by the mask, and its IFFT image
398 (Fig. 7g) revealed a single Mgh particle showing ($\bar{3}$11) and ($\bar{3}\bar{2}\bar{1}$) planes, with the angle
399 between the two facets being 64.4° (close to the theoretical value of 61.1°). Besides, in the
400 selected area "h" from Fig. 7a, another Mgh particle with the zone axis [$\bar{1}$3$\bar{3}$] was identified
401 by the FFT pattern (Fig. 7h). Moreover, a Hem particle along the zone axis [0$\bar{9}$3] could be
402 identified by the FFT pattern (Fig. 7i) from the selected area "i" of Fig. 7a, but the
403 crystallinity of the Hem particle in this sample was weaker as compared with that in Fh2-
404 Mnt1-400-4. As such, the heterogeneous phase transformation of Fh was also obtained for
405 Fh2/Mnt1-400-4.

406 To study the transformation characteristics of the heteroaggregates at the higher
407 temperature, both Fh2-Mnt1 and Fh2/Mnt1 were heated at 600°C for 1 h. TEM results
408 showed that the distribution of Fe and Si was more uniform on Fh2/Mnt1-600-1 than on
409 Fh2-Mnt1-600-1 (Fig. 8a and Fig. S8a-c), although the local accumulation of Fe and Si
410 could still be observed. According to the SAED results, the diffraction rings of Fh could
411 not be observed on Fh2-Mnt1-600-1, while the diffraction spots of Hem were recorded (Fig.
412 S8), suggesting the complete transformation of Fh to Hem. For Fh2/Mnt1-600-1, the
413 transformation of Fh was related to the local Fe content (i.e., Fh heterogeneity on Mnt). In
414 specific, the transformation of Fh was negligible in the area where the atomic ratio of Fe/Si
415 was low (i.e., 0.62), in which the diffraction rings of Fh were obvious (Fig. 8d). Besides,
416 the HRTEM image and FFT pattern in this area also did not show other crystalline iron
417 oxides (Fig. 8b). In the area where the atomic ratio of Fe/Si increased to 3.79, the SAED
418 pattern showed weak diffraction rings of Fh and the diffraction spots of Hem became
419 obvious (Fig. 8e). For the area with an even higher Fe/Si ratio (5.39), the diffraction rings
420 of Fh disappeared, and the formed particles were crystalline Hem with d values of 0.37,
421 0.25, 0.17, and 0.15 nm (Fig. 8f). Besides, the clear crystal fringes could be observed in
422 the HRTEM image with interplanar spacings of 0.22 and 0.27 nm (Fig. 8c), and the FFT
423 pattern indicated that Hem was along the zone axis [$1\bar{7}2$] (the inset in Fig. 8c).

424 Above TEM results, consistent with the macroscopic characterization results from
425 XRD, TG-DSC, and magnetism investigations, clearly demonstrated that Mnt could not
426 only retard the transformation of Fh but also lead to the heterogeneous phase
427 transformation of Fh. In general, the retardation effect of Fh transformation by Mnt is more
428 evident for the heteroaggregates with lower Fh contents and synthesized by in-situ growing

Fh on Mnt (i.e., Fh/Mnt). With proper heating temperature and duration, the heated heteroaggregates may simultaneously contain pristine Fh, intermediate Mgh, and transformed Hem. The underlying mechanisms for the retarded and heterogeneous phase transformation of Fh will be further discussed hereinafter.

DISCUSSION

The effects of surface interactions on the transformation of Fh

Numerous previous studies have concerned the stability and phase transformation of Fh in the nature (e.g., Kraal et al. 2019; Sheng et al. 2020, 2021). As a precursor of other crystalline iron (oxyhydr)oxides, Fh can spontaneously transform to Gth through dissolution-recrystallization (Das et al. 2011b) and oriented aggregation (Burleson and Penn. 2006), and to Hem by solid-state rearrangement (Towe and Bradley 1967; Yan et al. 2020). Some concurrent chemicals (e.g., Fe(II), silicate, and phosphate) may also induce the transformation of Fh to other iron (oxyhydr)oxides such as lepidocrocite, Mgh, or magnetite (Mag), as the concurrent chemicals can further affect the chemical components and aggregation states of Fh (Hansel et al. 2005; Liu et al. 2007; Cabello et al. 2009; Sheng et al. 2020). Above studies demonstrate that the phase transformation of Fh involves rather complex pathways and products. However, the dry-heating transformation conditions we applied in this work can only support the formation of Hem and Mgh, as it does not involve the release of ions from both Fh and Mnt. Nonetheless, the presence of Mnt still

448 significantly enhances the complexity of the transformation process, e.g., the retarded and
449 heterogeneous transformation process (Fig. 3-8).

450 Hem is the major and final transformed product in this work, and we will first discuss
451 the effects of Mnt on the transformation of Fh to Hem. Indeed, the transformation
452 mechanism of Fh to Hem, with or without the presence of concurrent chemicals, has been
453 well studied previously (Das et al. 2011a, b; Soltis et al. 2016; Jiang et al. 2018).
454 Structurally, Fh is primarily built from Fe (O, $OH)_6$ octahedra sharing corners and edges,
455 while Hem shares octahedra faces; as such, the transformation of Fh to Hem needs a
456 structural rearrangement (Cornell and Schwertmann 2003). Zhao et al. (1994) reported that
457 the dehydroxylation occurs at the interior of Fh particles, leading to charge imbalance and
458 structural strain. Then, Hem starts to form after reaching a point that the defects cannot be
459 tolerated and a structural rearrangement (e.g., formation of face-sharing of Fe polyhedron)
460 begins. Wang et al. (2015) suggested that after losing hydroxyl the aggregation of Fh
461 particles is vital to the formation of Hem. Navrotsky et al. (2008) proposed that the Fh
462 aggregates become thermodynamically unstable when their particle size is larger than ~8
463 nm during the dehydroxylated process. In this view, the transformation of Fh to Hem at
464 least involves aggregation, dehydroxylation, and structural rearrangement steps.
465 Concurrent chemicals, therefore, can affect the transformation process of Fh by influencing
466 these involved steps (Campell et al. 2002; Wang et al. 2015; Rzepa et al. 2016; Yan et al.

467 2020). Similarly, the complex transformation behaviors of Fh in this work should be
468 attributed to the influence of these transformation steps by Mnt. Unlike the studies by
469 Schwertmann et al (1988, 2000) in the hydrothermal system, the release of ions from Mnt
470 is excluded in our system. As such, the strong interactions between Fh and Mnt should be
471 the main reason influencing these transformation steps, and subsequently affecting the
472 transformation of Fh to Hem.

473 The strong interactions between Fh and Mnt, which mainly involve electrostatic
474 attraction, hydrogen bonding, and chemical bonding (as shown by FTIR analysis), can at
475 least affect the aggregation of Fh on Mnt and structural rearrangement of the
476 dehydroxylated Fh. As shown by the above characterization results, the strong interactions
477 between the two minerals, in combination with the large specific surface area of Mnt, can
478 well disperse Fh particles on Mnt (i.e., reducing the aggregation) for the synthesized
479 heteroaggregates (Fig. 9), particularly for Fh/Mnt (Fig. 1d-k). Besides, the strong
480 interactions, (chemical bonding in particular), theoretically can reduce the thermal mobility
481 of Fh particles during heating (i.e., maintaining their dispersion on Mnt), which in
482 combination with the physical separation effect of Mnt layers, would help inhibit the
483 aggregation of Fh particles during the transformation process. On the other hand, the
484 surface functional groups (e.g., Si/Al-OH) on Mnt, similar to many studied concurrent
485 chemicals (e.g., phosphate, silicate), can form stable chemical bonds with Fh. As

mentioned above, these chemical bonds (Al-O-Fe and Si-O-Fe) may increase the coordination symmetry of the Fe atom to enhance the stability of Fh, and limit the rearrangement of the Fe polyhedron of Fh (Zhao et al. 1994; Glasauer et al. 2000; Chen et al. 2022). With these influences caused by the interactions between Fh and Mnt, the transformation of Fh to Hem, therefore, is retarded by Mnt. Noticeably, the heteroaggregates with better dispersion of Fh and stronger surface interactions should have a stronger retarding effect on the transformation of Fh. These findings well explain our results that the Fh/Mnt heteroaggregates with a higher Mnt to Fh ratio are more effective in retarding the transformation of Fh and decreasing the particle size of the transformed Hem (Fig. 3 and 5).

We should notice that the complexity of Fh transformation in this work is more related to the heterogeneous transformation of Fh on these heteroaggregates (Fig 9b). Our TEM observations show the simultaneous presence of pristine Fh, intermediate Mgh, and transformed Hem on some heated heteroaggregates, and the transformation of Fh is closely related to the local Fe content on the heteroaggregates (Fig. 6-8). This should be attributed to the heterogeneous structure of these heteroaggregates, which then will significantly affect the surface interactions between Fh and Mnt. The heterogeneous structure arises from the uneven distribution of Fh on the Mnt surface (Fig. 9b), from both the lateral and vertical aspects. As the surface interactions will gradually decrease with the increment of

505 distance from the interface, only those Fh particles directly contacting with Mnt will most
506 strongly interact with Mnt (Fig. 9c). In this term, we can expect that the first layer of Fh
507 particles will be most effectively inhibited by Mnt during the transformation, while the
508 large Fh aggregates (e.g., those on Fh-Mnt with a high Fh to Mnt ratio) will be less inhibited,
509 i.e., behaving more likely as pure Fh (Fig. 9b). Between these two extreme situations are
510 those will be affected to different extents, depending on their distance from the interface.
511 For instance, Fh was well reserved in the area with low Fh content on Fh2/Mnt1-600-1(Fig.
512 8b and d), which can be attributed to the direct contact of most Fh with Mnt in this area
513 (i.e., strong surface interactions). While the more apparent transformation of Fh to Hem in
514 the area with a high Fe/Si ratio was observed (Fig. 8f), as most Fh in this area is within the
515 aggregates instead of in direct contact with the Mnt surface. Noticeably, as the surface
516 interactions between Fh and Mnt are the main factor that makes the transformation of Fh
517 on the heteroaggregates deviate from pure Fh, the Fh particles in direct contact with Mnt
518 should more likely involve in the heterogeneous transformation. Indeed, our results showed
519 that the heterogeneous transformation of Fh is more apparent on the heated Fh/Mnt than
520 on the heated Fh-Mnt (Fig. 8 and Fig. S8), in agreement with the much better coating of
521 Fh on Mnt for Fh/Mnt. In all, this study for the first time showed the heterogeneous
522 transformation of Fh on mineral surfaces. Considering the widespread occurrence of Fh on
523 mineral surfaces in the nature, we can expect that the heterogeneous transformation of Fh

524 should be very common.

525 As mentioned above, the heterogeneous structure of Fh/Mnt (or Fh-Mnt) and the
526 strong surface interactions between Fh and Mnt are the main factors causing the retarded
527 and heterogeneous transformation of Fh on these samples. Meanwhile, these factors, are
528 indeed determined by the synthetic methods of the heteroaggregates and the ratios of the
529 two mineral components. In general, better dispersion of Fh on Mnt and stronger surface
530 interactions between them are obtained on Fh/Mnt than on Fh-Mnt, and thus the retarded
531 and heterogeneous transformation of Fh particles is more apparent on Fh/Mnt. Similar
532 results can be obtained for the heteroaggregates with a higher Mnt to Fh ratio, as they have
533 a better surface coating and stronger surface interactions as well.

534 **Formation of Mgh during the transformation process**

535 Magnetic enhancement of topsoils and paleosols is thought to be related to the iron
536 (oxyhydr)oxides, especially Mgh and Mag (Ahmed and Maher 2018; Bilardello et al. 2020).
537 In this work, Mgh forms as an intermediate on the heated heteroaggregates during the dry-
538 heating transformation of Fh (Fig. 6 and 7), and results in the magnetic enhancement (Fig.
539 4). The transformation mechanism of Fh to Mgh has been reported by numerous studies
540 (Rzepa et al. 2016; Jiang et al. 2018; Pieczara et al. 2020). Aggregation, dehydroxylation,
541 and rearrangement are also thought as the necessary steps for the transformation of Fh to
542 Mgh due to their difference in chemical components and crystal structure (Cornell and

543 Schwertmann 2003). The different transformation pathways of Fh (to Hem or Mgh) are
544 closely related to the aggregation extent of the dehydroxylated Fh, which will be discussed
545 in detail hereinafter.

546 Generally, the formation of iron (oxyhydr)oxides is thermodynamically governed by
547 the Gibbs free energy, which is related to their particle size and increases in different slopes
548 with the decrement of particle size, leading to complex crossovers of different iron
549 (oxyhydr)oxides at the nanoscale (Navrotsky et al. 2008). Bulk Hem is generally the most
550 stable iron oxide and needs less Gibbs free energy for its formation. However, after the
551 particle size decreases to ~16 nm, less Gibbs free energy is needed for the formation of
552 ultrafine Mgh as compared with the formation of Hem, which suggest that the preferential
553 formation of Mgh with small particle size is thermodynamically favorable (Navrotsky et
554 al. 2008; Rzepa et al. 2016; Jiang et al. 2018). For example, Rzepa et al. (2016) reported
555 that the limited growth of Fh, due to the space restriction in the SiO_2 matrix, was beneficial
556 for Mgh formation. Jiang et al. (2018) also suggested that after large amounts of Fh
557 aggregates transformed to Hem, the remaining small amounts of Fh clusters would favor
558 the formation of ultrafine Mgh particles. Other explanations have been proposed for the
559 favorable transformation of Fh into Mgh as well. For example, several studies suggested
560 that the tetrahedrally coordinated Fe in Fh is indeed beneficial for the formation of Mgh,
561 due to the presence of Fe tetrahedra in Mgh as well (Mazzetti and Thistlethwaite 2002;

562 Michel et al. 2007b; Maillot et al. 2011; Guyodo et al. 2012). Besides, it is believed that
563 the adsorbed ligands on Fh could slow down the transformation of Fh to Hem, which then
564 might facilitate the formation of the intermediate mineral phase (i.e., Mgh) (Barron and
565 Torrent 2002; Barron et al. 2003; Cabello et al. 2009).

566 Interestingly, the heteroaggregates synthesized in this work can decrease the size of
567 Fh aggregates and slow down their transformation rate, which should benefit the formation
568 of Mgh (Fig. 9b). As shown by the above characterization results, the spatial separation of
569 Fh on Mnt and the surface interactions between the two components can decrease the size
570 of Fh aggregates on the heteroaggregates (Fig. 1), and limit the growth of dehydroxylated
571 Fh during the thermal treatment (Fig. 5). As such, thermodynamically the formation of
572 Mgh with small particle sizes is favorable during the transformation of Fh on the
573 heteroaggregates. This is consistent with the TEM results that the formed Mgh particles
574 have a rather small size (< 16 nm). In addition, as mentioned above, the chemical bonding
575 (i.e., Si-O-Fe/Al-O-Fe) formed between Fh and Mnt can retard the direct aggregation and
576 rearrangement of Fh to form Hem, and thus slow down the transformation rate. In this term,
577 the formation of Mgh can be triggered by the Fe tetrahedra in the Fh structure.

578 Mgh can transform to more stable Hem in the nature, but this process may be inhibited
579 when the grain size of Mgh is smaller than ~16 nm, or when strong interactions present
580 between Mgh and concurrent matters (Ramesh et al. 2000; Navrotsky et al. 2008; El

581 Mendili et al. 2012). For example, Ramesh et al. (2000) reported that the formation of
582 hydrogen bonds between the hydrated surface of SiO_2 and the adsorbed Mgh nanoparticles
583 would retard their transformation to Hem. In our work, the decrease of χ on Fh2-Mnt1 after
584 2 h's heating at 400°C could be contributed to the transformation of Mgh to Hem, while,
585 the nearly stable χ of heated Fh2/Mnt1 should be ascribed to the preservation of Mgh by
586 Mnt (Fig. 4). The above characterization results well demonstrate the better dispersion of
587 Fh particles and stronger surface interactions between the two mineral components on
588 Fh2/Mnt1, and thus we can expect a smaller grain size of the generated Mgh and its
589 stronger interactions with Mnt on Fh2/Mnt1. As a result, the generated Mgh can transform
590 to Hem on Fh2-Mnt1 while being well preserved on Fh2/Mnt1. These results demonstrate
591 that the surface interactions not only dictate the transformation of Fh to Mgh but also
592 influence the stability of the generated Mgh. Our results well demonstrate that the surface
593 interactions between minerals will contribute to the generation and preservation of
594 NMMNs.

595 **IMPLICATIONS**

596 This work, for the first time, studied the effect of surface interactions between Fh and
597 Mnt on the transformation behaviors of Fh under nonaqueous environments, and the
598 findings have at least the following multiple implications. Firstly, this work provides novel
599 information for understanding the phase transformation of Fh under widespread
600 nonaqueous environments, particularly during the high temperature geochemistry

processes, e.g., wildfire. The strong surface interactions between Fh and Mnt cause both retarded and heterogeneous transformation of Fh within the heteroaggregates under heated nonaqueous environments, which differs from the aqueous transformation processes in rate, products, and pathways, etc. Besides, the applied high temperature can not only simulate the environments affected by wildfire, but also accelerate the Fh transformation process (i.e., cutting the geological timescale into laboratory timescale), which will help understand the transformation behaviors of Fh under mild and drying environments as well.

The findings of this work also suggest that clay minerals can play important role in stabilizing NMMNs in the nature. NMMNs are ubiquitous in the Earth's surface and near-surface environment (Hochella et al. 2019). Indeed, almost all crystals will pass through the nanocrystal stage during their formation, but the stage is highly transitory in many geological settings (Banfield and Zhang 2001). As such, NMMNs are always unstable unless they are stabilized by interacting with concurrent chemicals or forming heteroaggregates (Hochella et al. 2019; Yan et al. 2021). This study shows that Mnt can well stabilize Fh through strong surface interactions and spatial dispersion. Besides, the heterogeneous transformation of Fh (i.e., the simultaneous presence of Fh, Mgh, and Hem) also suggests that the concurrent Mnt will result in more complex heteroaggregations in the nature. Considering the wide coexistence of iron (oxyhydr)oxides and clay minerals in multiple geological settings and the strong interactions between them, we can expect that clay minerals are conducive to the generation and long-term stabilization of various iron (oxyhydr)oxides NMMNs, resulting in the formation of various heteroaggregates of these minerals. Similarly, because of the large abundance and widespread of clay minerals in the nature, one can propose that clay minerals may help to stabilize other NMMNs as well.

624 Moreover, this work provides another good example showing the special function of
625 clay minerals as a natural stabilizer in preserving/protecting concurrent chemicals/matters.
626 Clay minerals are mainly composed of chemically inert aluminosilicates nanolayers, which
627 in combination with their large abundance and good surface sorption capacity make them
628 excellent natural stabilizers for many environmental chemicals (Su et al. 2016; Loganathan
629 et al. 2020). Indeed, numerous studies have shown that clay minerals can well
630 preserve/protect soil organic matters (Loganathan et al. 2020), biomolecules (Torti et al.
631 2015), microbes (Hassard et al. 2016), and plant/animal residues (Singh et al. 2019), which
632 is vital to many important geological and geochemical processes, such as the origin and
633 evolution of life on earth (Fomina and Skorochod 2020), the global cycling of carbon
634 (Morrissey et al. 2015), the formation of crude oils (Wu et al. 2012), and the formation of
635 well-preserved fossils(Anderson et al. 2018; McMahon et al. 2018). This work showed that
636 Mnt as typical clay minerals can stabilize Fh nanoparticles (and likely other NMMNs as
637 well) in the nature by retarding its phase transformation, and thus it can be another good
638 example supporting the special function of clay minerals as a natural stabilizer.
639 Finally, this work also demonstrates a possible pathway for the genesis of Mgh in the
640 nature. It has been reported that the Mgh always coexists with Hem in the nature and forms
641 from Fh in the laboratory in the presence of organic matter or other inorganic ligands during
642 the nonaqueous transformation (i.e., silicate and phosphate) (Campbell et al. 1997; Rzepa
643 et al. 2016; Pieczara et al. 2020). Our study shows that Mgh could be an intermediate
644 mineral phase during the thermal treatment of Fh in the presence of Mnt, which may be
645 another explanation for the enhancement of soil magnetism during the pedogenic process
646 or after a wildfire, because of the widespread coexistence of Fh and clay minerals in the

near-surface environment (Dimirkou et al. 2002; Zeng et al. 2020). In addition, Fh and Mnt are also important soil mineral components on Mars (Bishop et al. 1993). Hence, the magnetism enhancement on Mars might be explained by the formation of Mgh during the transformation of Fh in the presence of Mnt.

ACKNOWLEDGEMENTS AND FUNDING

This study was supported by the Guangdong Major Project of Basic and Applied Basic Research (Grant No. 2019B030302013), National Natural Science Foundation of China (Grant Nos. 41921003, 41872044, and 41902040), China National Funds for Distinguished Young Scientists (Grant No. 41825003), Youth Innovation Promotion Association CAS (Grant No. 2020347), and Science and Technology Planning Project of Guangdong Province, China (Grant No. 2020B1212060055).

REFERENCES CITED

Ahmed, I.A.M., and Maher, B.A. (2018) Identification and paleoclimatic significance of magnetite nanoparticles in soils. Proceedings of the National Academy of Science of the United States of America, 115, 1736-1741.

Anderson, R.P., Tosca, N.J., Gaines, R.R., Koch, N.M., and Briggs, D.E.G. (2018) A mineralogical signature for Burgess shale-type fossilization. Geology, 46, 347-350.

Banfield, J.F., and Zhang, H.Z. (2001) Nanoparticles and the environment. Reviews in Mineralogy & Geochemistry, 44, 1-58.

Barron, V., and Torrent, J. (2002) Evidence for a simple pathway to maghemite in Earth and Mars soils. Geochimica et Cosmochimica Acta, 66, 2801-2806.

Barron, V., Torrent, J., and de Grave, E. (2003) Hydromaghemite, an intermediate in the hydrothermal transformation of 2-line ferrihydrite into hematite. American Mineralogist, 88, 1679-1688.

Bilardello, D., Banerjee, S.K., Volk Michael, W.R., Soltis, J.A., and Penn, R.L. (2020) Simulation of natural iron oxides alteration in soil: conversion of synthetic ferrihydrite to hematite without artificial dopants, observed with magnetic methods. Geochemistry Geophysics Geosystems, 21, e2020GC009037.

Bishop, J.L., Pieters, C.M., and Burns, R.G. (1993) Reflectance and mossbauer-spectroscopy of ferrihydrite-montmorillonite assemblages as Mars soil analog materials. Geochimica et Cosmochimica Acta, 57, 4583-4595.

Bowman, D.M.J.S., Balch, J.K., Artaxo, P., Bond, W.J., Carlson, J.M., Cochrane, M.A., D'Antonio, C.M., DeFries, R.S., Doyle, J.C., Harrison, S.P., and others. (2009) Fire in the Earth system. Science, 324, 481-484.

Burleson, D.J., and Penn, R.L. (2006) Two-step growth of goethite from ferrihydrite. Langmuir, 22, 402-409.

Cabello, E., Morales, M.P., Serna, C.J., Barrón, V., and Torrent, J. (2009) Magnetic Enhancement

During the Crystallization of Ferrihydrite at 25 and 50°C. Clays and Clay Minerals, 57, 46-53.

Campbell, A.S., Schwertmann, U., and Campbell, P.A. (1997) Formation of cubic phases on heating ferrihydrite. Clay Minerals, 32, 615-622.

Campell, A.S., Schwertmann, U., Stanjek, H., Friedl, J., Kyek, A., and Campbell, P.A. (2002) Si incorporation into hematite by heating Si-ferrihydrite. Langmuir, 18, 7804-7809.

Celis, R., Cornejo, J., and Hermosin, M.C. (1998) Textural properties of synthetic clay-ferrihydrite associations. Clay Minerals, 33, 395-407.

Certini, G. (2005) Effects of fire on properties of forest soils: a review. Oecologia, 143, 1–10.

Chen, L., Wang, H., Sun, Y.P., Zhao, Y., and Shi, H.X. (2022) Interface mechanisms of the catalytic ozonation of humic acids over siliceous ferrihydrite: Morphology, stability, and the catalytic process. Environmental Research, 203, 111870.

Cornell, R.M., and Schwertmann, U. (2003) The iron oxides: structure, properties, reactions, occurrences, and uses. Wiley-VCH, Weinheim.

Das, S., Hendry, M.J., and Essilfie-Dughan, J. (2011a) Effects of Adsorbed Arsenate on the Rate of Transformation of 2-Line Ferrihydrite at pH 10. Environmental Science & Technology, 45, 5557-5563.

Das, S., Hendry, M.J., and Essilfie-Dughan, J. (2011b) Transformation of Two-Line Ferrihydrite to Goethite and Hematite as a Function of pH and Temperature. Environmental Science & Technology, 45, 268-275.

Dimirkou, A., Ioannou, A., and Doula, M. (2002) Preparation, characterization and sorption properties for phosphates of hematite, bentonite and bentonite-hematite systems. Advances in Colloid and Interface Science, 97, 37-61.

Dong, C., Williams, A.P., Abatzoglou, J.T., Lin, K., Okin, G.S., Gillespie, T.W., Long, D., Lin, Y.H., Hall, A., and MacDonald, G.M. (2022) The season for large fires in Southern California is projected to lengthen in a changing climate. Communication Earth & Environment, 3, s43247-022-00344-6.

El Mendili, Y., Bardeau, J.F., Randrianantoandro, N., Grasset, F., and Greneche, J.M. (2012) Insights into the Mechanism Related to the Phase Transition from gamma-Fe_2O_3 to alpha-Fe_2O_3

712 Nanoparticles Induced by Thermal Treatment and Laser Irradiation. Journal of Physical
713 Chemistry C, 116, 23785-23792.
714 Fomina, M., and Skorochod, I. (2020) Microbial interaction with clay minerals and its
715 environmental and biotechnological implications. Minerals, 10, 861.
716 Francisco, P.C.M., Sato, T., Otake, T., and Kasama, T. (2016) Kinetics of Fe^{3+} mineral crystallization
717 from ferrihydrite in the presence of Si at alkaline conditions and implications for nuclear waste
718 disposal. American Mineralogist, 101, 2057-2069.
719 Francisco, P.C.M., Sato, T., Otake, T., Kasama, T., Suzuki, S., Shiwaku, H., and Yaita, T. (2018)
720 Mechanisms of Se(IV) Coprecipitation with Ferrihydrite at Acidic and Alkaline Conditions and
721 Its Behavior during Aging. Environmental Science & Technology, 52, 4817-4826.
722 Gibson, C.M., Chasmer, L.E., Thompson, D.K., Quinton, W.L., Flannigan, M.D., and Olefeldt, D.
723 (2018) Wildfire as a major driver of recent permafrost thaw in boreal peatlands. Nature
724 Communication, 9, 3041.
725 Girona, T., Realmuto, V., and Lundgren, P. (2021) Large-scale thermal unrest of volcanoes for years
726 prior to eruption. Nature Geoscience, 14, 238-241.
727 Glasauer, S.M., Hug, P., Weidler, P.G., and Gehring, A.U. (2000) Inhibition of sintering by Si during
728 the conversion of Si-rich ferrihydrite to hematite. Clays and Clay Minerals, 48, 51-56.
729 Guggenheim, S., and van Groos, A.F.K. (2001) Baseline studies of The Clay Minerals Society
730 Source Clays: Thermal analysis. Clays and Clay Minerals, 49, 433-443.
731 Guyodo, Y., Sainctavit, P., Arrio, M.A., Carvallo, C., Lee Penn, R., Erbs, J.J., Forsberg, B.S., Morin,
732 G., Maillot, F., Lagroix, F., and others. (2012) X-ray magnetic circular dichroïsm provides
733 strong evidence for tetrahedral iron in ferrihydrite. Geochemistry Geophysics Geosystems, 13,
734 Q06Z44.
735 Hansel, C.M., Benner, S.G., and Fendorf, S. (2005) Competing Fe(II)-induced mineralization
736 pathways of ferrihydrite. Environmental Science & Technology, 39, 7147-7153.
737 Hassard, F., Gwyther, C.L., Farkas, K., Andrews, A., Jones, V., Cox, B., Brett, H., Jones, D.L.,
738 McDonald, J.E., and Malham, S.K. (2016) Abundance and distribution of enteric bacteria and

viruses in coastal and estuarine sediments- a review. Microbiol, 7, 1692.

Hassellov, Y., and Lecerf, A. (2006) The transformation of ferrihydrite into goethite or hematite, revisited. Journal of Solid State Chemistry, 179, 716-722.

Hassellov, M., and von der Kammer, F. (2008) Iron Oxides as Geochemical Nanovectors for Metal Transport in Soil-River Systems. Elements, 4, 401-406.

He, H.P., Yang, Y.P., Ma, L.Y., Su, X.L., Xian, H.Y., Zhu, J.X., Teng, H.H., and Guggenheim, S. (2021) Evidence for a two-stage particle attachment mechanism for phyllosilicate crystallization in geochemical process. American Mineralogy, 106, 983-993.

Hochella, M.F. Jr., Kasama, T., Putnis, A., Putnis, C.V., and Moore, J.N. (2005) Environmentally important, poorly crystalline Fe/Mn hydrous oxides: ferrihydrite and a possibly new vernadite-like mineral from the Clark Fork River Superfund Complex. American Mineralogist, 90, 718-724.

Hochella, M.F., Jr., Lower, S.K., Maurice, P.A., Penn, R.L., Sahai, N., Sparks, D.L., and Twining, B.S. (2008) Nanominerals, mineral nanoparticles, and Earth systems. Science, 319, 1631-1635.

Hochella, M.F., Jr., Mogk, D.W., Ranville, J., Allen, I.C., Luther, G.W., Marr, L.C., McGrail, B.P., Murayama, M., Qafoku, N.P., Rosso, K.M., and others. (2019) Natural, incidental, and engineered nanomaterials and their impacts on the Earth system. Science, 363, 1414-+.

Jambor, J.L., and Dutrizac, J.E. (1998) Occurrence and constitution of natural and synthetic ferrihydrite, a widespread iron oxyhydroxide. Chemical Reviews, 98, 2549-2585.

Jiang, Z.X., Liu, Q.Q., Roberts, A.P., Barrón, V., Torrent, J., and Zhang, Q. (2018) A new model for transformation of ferrihydrite to hematite in soils and sediments. Geology, 46, 987-990.

Johnston, S.G., Bennett, W.W., Burton, E.D., Hockmann, K., Dawson, N., and Karimian, N. (2018) Rapid arsenic(V)-reduction by fire in schwertmannite-rich soil enhances arsenic mobilisation. Geochimica et Cosmochimica Acta, 227, 1-18.

Khaorapapong, N., Ontam, A., and Ogawa, M. (2010) Formation of ZnS and CdS in the interlayer spaces of montmorillonite. Applied Clay Science, 50, 19-24.

Kraal, P., van Genuchten, C.M., Behrends, T., and Rose, A.L. (2019) Sorption of phosphate and silicate alters dissolution kinetics of poorly crystalline iron (oxyhydr)oxide. Chemosphere, 234,

690-701.

Lewis, D.G. (1992) Transformation induced in ferrihydrite by oven-drying. Zeitschrift fur Pflanzenernahrung und Bodenkunde, 155, 461-466.

Li, Y., Yang, M.J., Pentrak, M., He, H.P., and Arai, Y. (2020) Carbonate-Enhanced Transformation of Ferrihydrite to Hematite. Environmental Science & Technology, 54, 13701-13708.

Liang, C.W., Fu, F.L., and Tang, B. (2021) Mn-incorporated ferrihydrite for Cr(VI) immobilization: Adsorption behavior and the fate of Cr(VI) during aging. Journal of Hazardous Materials, 417, 126073.

Liu, H., Li, P., Zhu, M.Y., Wei, Y., and Sun, Y.H. (2007) Fe(II)-induced transformation from ferrihydrite to lepidocrocite and goethite. Journal of Solid State Chemistry, 180, 2121-2128.

Liu, H., Jiang, G.M., Zhuang H.Y., and Wang, K.J. (2008) Distribution, utilization structure and potential of biomass resources in rural China: With special references of crop residues. Renewable & Sustainable Energy Reviews, 12, 1402-1418.

Liu, J., Zhu, R.L., Liang, X.L., Ma, L.Y., Lin, X.J., Zhu, J.X., He, H.P., Parker, S.C., and Molinari, M. (2018) Synergistic adsorption of Cd(II) with sulfate/phosphate on ferrihydrite: An in situ ATR-FTIR/2D-COS study. Chemical Geology, 477, 12-21.

Liu, J., Inoué, S., Zhu, R.L., He, H.P., and Hochella, M.F. Jr. (2021a) Facet-specific oxidation of Mn(II) and heterogeneous growth of manganese (oxyhydr)oxides on hematite nanoparticles. Geochimica et Cosmochimica Acta, 307, 151-167.

Liu, J., Zhu, R.L., Ma, L.Y., Fu, H.Y., Lin, X.J., Parker, S.C., and Molinari, M. (2021b) Adsorption of phosphate and cadmium on iron (oxyhydr)oxides: A comparative study on ferrihydrite, goethite, and hematite. Geodeima, 383, 114799.

Loan, M., Parkinson, G.M., and Richmond, W.R. (2005) The effect of zinc sulfide on phase transformation of ferrihydrite. American Mineralogist, 90, 258-261.

Loehr, S.C., Murphy, D.T., Nothdurft, L.D., Bolhar, R., Piazolo, S., and Siegel, C. (2017) Maghemite soil nodules reveal the impact of fire on mineralogical and geochemical differentiation at the Earth's surface. Geochimica et Cosmochimica Acta, 200, 25-41.

Loganathan, N., Ferguson, B.O., Arey, B., Argersinger, H.E., and Bowers, G.M. (2020) A

mechanistic exploration of natural organic matter aggregation and surface complexation in smectite mesopores. Journal of Physical Chemistry A, 124, 9832-9843.

Lizundia-Loiola, J., Oton, G., Ramo, R., and Chuvieco, E.A. (2020) A spatio-temperal active-fire clustering approach for global burned area mapping at 250 m from MODIS data. Remote Sensing of Environment, 236, 111493.

Maillot, F., Morin, G., Wang, Y., Bonnin, D., Ildefonse, P., Chaneac, C., and Calas, G. (2011) New insight into the structure of nanocrystalline ferrihydrite: EXAFS evidence for tetrahedrally coordinated iron(III). Geochimica et Cosmochimica Acta, 75, 2708-2720.

Mazzetti, L., and Thistlethwaite, P.J. (2002) Raman spectra and thermal transformations of ferrihydrite and schwertmannite. Journal of Raman Spectroscopy, 33, 104-111.

McMahon, S., Bosak, T., Grotzinger, J.P., Milliken, R.E., Summons, R.E., Daye, M., Newman, S.A., Fraeman, A., Williford, K.H., and Briggs, D.E.G. (2018) A field guide to finding fossils on Mars. Journal of Geophysical Research: Planets, 123, 1012-1040.

Michel, F.M., Ehm, L., Liu, G., Han, W.Q., Antao, S.M., Chupas, P.J., Lee, P.L., Knorr, K., Eulert, H., Kim, J., and others. (2007a) Similarities in 2-and 6-line ferrihydrite based on pair distribution function analysis of X-ray total scattering. Chemistry of Materials, 19, 1489-1496.

Michel, F.M., Ehm, L., Antao, S.M., Lee, P.L., Chupas, P.J., Liu, G., Strongin, D.R., Schoonen, M.A.A., Phillips, B.L., and Parise, J.B. (2007b) The structure of ferrihydrite, a nanocrystalline material. Science, 316, 1726-1729.

Morrissey, E.M., McHugh, T.A., Preteska, L., Hayer, M., Dijkstra, P., Hungate, B.A., and Schwartz, E. (2015) Dynamics of extracellular DNA decomposition and bacterial community composition in soil. Soil Biology & Biochemistry, 86, 42-49.

Navrotsky, A., Mazeina, L., and Majzlan, J. (2008) Size-driven structural and thermodynamic complexity in iron oxides. Science, 319, 1635-1638.

Navrotsky, A., Ma, C., Lilova, K., and Birkner, N. (2010) Nanophase transition metal oxides show large thermodynamically driven shifts in oxidation-reduction equilibria. Science, 330, 199-201.

Pentrak, M., Hronsky, V., Palkova, H., Uhlik, P., Komadel, P., and Madejova, J. (2018) Alteration

of fine fraction of bentonite from Kopernica (Slovakia) under acid treatment: A combined XRD, FTIR, MAS NMR and AES study. Applied Clay Science, 163, 204-213.

Pieczara, G., Manecki, M., Rzepa, G., Borkiewicz, O., and Gawel, A. (2020) Thermal Stability and Decomposition Products of P-Doped Ferrihydrite. Materials, 13, 4113.

Pokrovski, G.S., Schott, J., Garges, F., and Hazemann, J.L. (2003) Iron (III)-silica interactions in aqueous solution: Insights from X-ray absorption fine structure spectroscopy. Geochimica et Cosmochimica Acta, 67, 3559-3573.

Putnis, A. (2014) Why Mineral Interfaces Matter. Science, 343, 1441-1442.

Raiswell, R., and Canfield, D.E. (2012) The iron biogeochemical cycle past and present. Geochemical Perspectives, 1, 1-220.

Ramesh, S., Felner, I., Koltypin, Y., and Gedanken, A. (2000) Reaction pathways at the iron-microspherical silica interface: Mechanistic aspects of the formation of target iron oxide phases. Journal of Materials Research, 15, 944-950.

Rzepa, G., Pieczara, G., Gawel, A., Tomczyk, A., and Zalecki, R. (2016) The influence of silicate on transformation pathways of synthetic 2-line ferrihydrite. Journal of Thermal Analysis and Calorimetry, 125, 407-421.

Schwertmann, U. (1979) Influence of aluminum on iron-oxides.5. clay-minerals as sources of aluminum. Soil Science, 128, 195-200.

Schwertmann, U. (1988) Goethite and hematite formation in the presence of clay-minerals and gibbsite at 25°C. Soil Science Society of America Journal, 52, 288-291.

Schwertmann, U., Friedl, J., Stanjek, H., and Schulze, D.G. (2000) The effect of clay minerals on the formation of goethite and hematite from ferrihydrite after 16 years' ageing at 25 degrees C and pH 4-7. Clay Minerals, 35, 613-623.

Sheng, A.X., Liu, J., Li, X.X., Qafoku, O., Collins, R.N., Jones, A.M., Pearce, C.I., Wang, C.M., Ni, J.R., Lu, A.H., and others. (2020) Labile Fe(III) from sorbed Fe(II) oxidation is the key intermediate in Fe(II)-catalyzed ferrihydrite transformation. Geochimica et Cosmochimica Acta, 272, 105-120.

Sheng, A.X., Liu, J., Li, X.X., Luo, L.L., Ding, Y.F., Chen, C.M., Zhang, X., Wang, C.M., and Rosso,

K.M. (2021) Labile Fe(III) supersaturation controls nucleation and properties of product phases from Fe(II)-catalyzed ferrihydrite transformation. Geochimica et Cosmochimica Acta, 309, 272-285.

Shi, K., and Touge, Y. (2022) Characterization of global wildfire burned area spatiotemporal patterns and underlying climate causes. Scientific reports, 12, s41598-021-04726-2.

Shu, Z.P., Liu, L.H., Qiu, G.H., Yang, X., Zhang, M.Z., Tan, W.F., Liu, C.S., and Wu, F. (2019) Photochemical Formation Process of Schwertmannite on Montmorillonite and Corresponding Cr(VI) Adsorption Capacity. Acs Earth and Space Chemistry, 3, 718-727.

Singh, M., Sarkar, B., Bolan, N.S., Ok, Y.S., and Churchman, G.J. (2019) Decomposition of soil organic matter as affected by clay types, pedogenic oxides and plant residue addition rates. Journal of Hazardous Materials, 15, 11-15

Soltis, J.A., Feinberg, J.M., Gilbert, B., and Penn, R.L. (2016) Phase transformation and particle-mediated growth in the formation of hematite from 2-line ferrihydrite. Crystal Growth & design, 16, 922-932.

Su, X.L., Ma, L.Y., Wei, J.M., and Zhu, R.L. (2016) Structure and thermal stability of organo-vermiculite. Applied Clay Science, 132, 261-266.

Sun, G.Z., Fu, F.L., and Tang, B. (2021) Fate of metal-EDTA complexes during ferrihydrite aging: Interaction of metal-EDTA and iron oxides. Chemosphere, 291, 132791.

Tang, W., Llort, J., Weis, J., Perron, M.M.G., Basart, S., Li, Z., Sathyendranath, S., Jackson, T., Rodriguez, E.S., Proemse, B.C., and others. (2020) Widespread phytoplankton blooms triggered by 2019-2020 Australian wildfires. Nature, 597, 370-+.

Terzano, R., Rascio, I., Allegretta, I., Porfido, C., Spagnuolo, M., Khanghahi, M.Y., Crecchio, C., Sakellariadou, F., and Gattullo, C.E. (2021) Fire effects on the distribution and bioavailability of potentially toxic elements (PTEs) in agricultural soils. Chemosphere, 281, 130752.

Torti, A., Lever, M.A., and Jorgensen, B.B. (2015) Origin, dynamics, and implications of extracellular DNA pools in marine sediments. Marine Genomics, 24, 185-196.

Towe, K.M., and Bradley, W.F. (1967) Mineralogical constitution of colloidal hydrous ferric oxides. Journal of Colloid and Interface Science, 24, 384-&.

878 Wang, J., and Liu, Z.Y. (2013) Preparation and Characterization of Acrylic Acid-Ca-
879 Montmorillonite and Its Application for Preparation of Poly(vinyl acetate)/Montmorillonite
880 Nanocomposite Emulsion by in situ Emulsion Polymerization. Asian Journal of Chemistry, 25,
881 5935-5940.
882 Wang, Z.H., Xiao, D.X., Bush, R.T., and Liu, J.S. (2015) Coprecipitated arsenate inhibits thermal
883 transformation of 2-line ferrihydrite: Implications for long-term stability of ferrihydrite.
884 Chemosphere, 122, 88-93.
885 Wei, S.Y., Tan, W.F., Zhao, W., Yu, Y.T., Liu, F., and Koopal, L.K. (2012) Microstructure, Interaction
886 Mechanisms, and Stability of Binary Systems Containing Goethite and Kaolinite. Soil Science
887 Society of America Journal, 76, 389-398.
888 Wu, L.M., Zhou, C.H., Keeling, J., Tong, D.S., and Yu, W.H. (2012) Towards an understanding of
889 the role of clay minerals in crude oil formation, migration and accumulation. Earth-Science
890 Review, 115, 373-386.
891 Xu, T.Y., Zhu, R.L., Zhu, G.Q., Zhu, J.X., Liang, X.L., Zhu, Y.P., and He, H.P. (2017) Mechanisms
892 for the enhanced photo-Fenton activity of ferrihydrite modified with $BiVO_4$ at neutral pH.
893 Applied Catalysis B: Environmental, 212, 50-58.
894 Yan, L.X., Zhu, R.L., Liu, J., Yang, Y.X., Zhu, J.X., Sun, H.J., and He, H.P. (2020) Effects of Fullerol
895 and Graphene Oxide on the Phase Transformation of Two-Line Ferrihydrite. Acs Earth and
896 Space Chemistry, 4, 335-344.
897 Yan, L.X., Chen, Q.Z., Yang, Y.X., and Zhu, R.L. (2021) The significant role of montmorillonite on
898 the formation of hematite nanoparticles from ferrihydrite under heat treatment. Applied Clay
899 Science, 202, 105962.
900 Yang, M.J., Liang, X.L., Li, Y., He, H.P., Zhu, R.L., and Arai, Y. (2021) Ferrihydrite transformation
901 impacted by adsorption and structural incorporation of rare earth elements. Acs Earth and
902 Space Chemistry, 5, 2768-2777.
903 Ye, W., Zhao, B.X., Gao, H., Huang, J.J., and Zhang, X.L. (2016) Preparation of highly efficient
904 and stable Fe,Zn,Al-pillared montmorillonite as heterogeneous catalyst for catalytic wet
905 peroxide oxidation of Orange II. Journal of Porous Materials, 23, 301-310.

Ye, C.J., Ariya, P.A., Fu, F.L., Yu, G.D., and Tang, B. (2021) Influence of Al(III) and Sb(V) on the transformation of ferrihydrite nanoparticles: Interaction among ferrihydrite, coprecipitated Al(III) and Sb (V). Journal of Hazardous Materials, 408, 124423.

Yee, N., Shaw, S., Benning, L.G., and Nguyen, T.H. (2006) The rate of ferrihydrite transformation to goethite via the Fe(II) pathway. American Mineralogist, 91, 92-96.

Yusiharni, E., and Gilkes, R.J. (2012) Changes in the mineralogy and chemistry of a lateritic soil due to a bushfire at Wundowie, Darling Range, Western Australia. Geoderma, 191, 140-150.

Yu, G.D., Fu, F.L., Ye, C.J., and Tang B. (2020) Behaviors and fate of adsorbed Cr(VI) during Fe(II)-induced transformation of ferrihydrite-humic acid co-precipitates. Journal of Hazardous Materials, 392, 122272.

Yuan, P., Annabi-Bergaya, F., Tao, Q., Fan, M.D., Liu, Z.W., Zhu, J.X., He, H.P., and Chen, T.H. (2008) A combined study by XRD, FTIR, TG and HRTEM on the structure of delaminated Fe-intercalated/pillared clay. Journal of Colloid and Interface Science, 324, 142-149.

Zeng, Q., Huang, L.Q., Ma, J.Y., Zhu, Z.H., He, C., Shi, Q., Liu, W., Wang, X., Xia, Q.Y., and Dong, H.L. (2020) Bio-reduction of ferrihydrite-montmorillonite-organic matter complexes: Effect of montmorillonite and fate of organic matter. Geochimica et Cosmochimica Acta, 276, 327-344.

Zhao, J.M., Huggins, F.E., Feng, Z., and Huffman, G.P. (1994) Ferrihydrite surface structure and its effects on phase transformation. Clays and Clay Minerals, 42, 737-746.

Zhu, G.M., Sushko, M.L., Loring, J.S., Legg, B.A., Song, M., Soltis, J.A., Huang, X.P., Rosso, K.M., and De Yoreo, J.J. (2021) Self-similar mesocrystals form via interface-driven nucleation and assembly. Nature, 590, 416-422.

Zhu, Y.P., Xie, Q.R., Zhu, R.L., Lv, Y., Xi, Y.F., Zhu, J.X., and Fan, J. (2022) Hydrothermal carbons/ferrihydrite heterogeneous Fenton catalysts with low H_2O_2 consumption and the effect of graphitization degrees. Chemosphere, 287, 131933.

FIGURE CAPTIONS

Figure 1. Structural characteristics of different samples before heating. XRD patterns of **(a)** Fh and Mnt, **(b)** Fh-Mnt, and **(c)** Fh/Mnt. SEM images of **(d)** Fh, **(e)** Fh2-Mnt1, **(f)** Fh1-Mnt1, and **(g)** Fh2/Mnt1. TEM images of **(h)** Fh, **(i)** Fh2-Mnt1, **(j)** Fh1-Mnt1, and **(k)** Fh2/Mnt1. The insets in h and k represent the SAED of the samples including 2-line Fh with two diffraction rings at d = 0.25 and 0.15 nm.

Figure 2. (a) TG curves of Mnt, Fh2-Mnt1, Fh 2/Mnt1, and Fh. **(b)** DSC curves of Mnt, Fh2-Mnt1, Fh2/Mnt1, and Fh. The dotted lines in **a** represent the theoretical TG curves of Fh and Mnt with a ratio of 2:1.

Figure 3. (a) XRD patterns of Fh-Mnt and Fh/Mnt after heating at 400°C for 4 h. **(b)** XRD patterns of Fh2-Mnt1and Fh2/Mnt1 after heating at different temperatures for 1 h. **(c)** XRD patterns of heating-treated Fh2-Mnt1 and Fh2/Mnt1 for different times at 400°C. **(d)** The dissolution of Fh by ammonium oxalate in Fh-Mnt and Fh/Mnt at different ratios after heating at 400°C for different times, and the Fe_o/Fe_t represents the residual content of Fh. 2Fh:1Mnt represents the mass ratio of Fh and Mnt is 2:1 in the heteroaggregates, and the similar meaning is expressed by 1Fh:1Mnt and 1Fh:2Mnt. The Fh in Fh/Mnt only underwent a slight transformation under these conditions, so only Fh2/Mnt1-400-4 was tested for dissolution to determine the degree of transformation.

950 **Figure 4.** The magnetic susceptibility (χ) of Fh, Mnt, Fh2-Mnt1, and Fh2/Mnt1 after
951 heating at 400°C at different time intervals. The lines are drawn for eye guidance.

952 **Figure 5.** The morphology features of different samples after heating at 400°C for 4 h.
953 SEM and TEM images of **(a-c)** Fh-400-4, **(d-f)** Fh2-Mnt1-400-4, **(g-i)** Fh1-Mnt1-400-
954 4, and **(j-l)** Fh2/Mnt1-400-4. Insets in **b**, **e**, and **h**, are the size distribution histograms
955 of particles in the corresponding images, with average particle sizes being calculated.
956 Inset in **k** represents the corresponding SAED showing Fh with two rings. Some of the
957 identified disparate particles are highlighted using different colors in **f** and **i**.

958 **Figure 6.** Detailed analysis of HRTEM images of Fh2-Mnt1-400-4. **(a)** HRTEM image.
959 **(b and c)** FFT pattern of the marked area in **a**, indicating that the marked area "b" and
960 "c" are Hem particles. **(d)** FFT pattern generated from marked area "d" in "a",
961 indicating the presence of Mgh along the zone axis $[\bar{1}2\bar{2}]$ and Hem along the zone axis
962 $[\bar{2}2\bar{1}]$ and $[4\bar{4}\bar{1}]$. **(e)** FFT pattern with the spots related to Mgh along the zone axis $[\bar{1}2\bar{2}]$
963 reserved. **(f)** IFFT image of **e**. The lattice fringes are attributed to the (210) and (011)
964 planes of Mgh. **(g and i)** the enlarge of marked area "g" and "i" in **a**. **(h and j)** the FFT
965 pattern of the yellow solid box in **g** and **i**, showing Mgh particles (marked with the
966 yellow dotted line in **g** and **i**) along the zone axis $[\bar{1}11]$ and $[02\bar{2}]$, respectively.

967 **Figure 7.** Detailed analysis of the HRTEM image of Fh2/Mnt1-400-4. **(a)** HRTEM
968 image. **(b and c)** FFT pattern of the marked areas of "b" and "c" in **a**, revealing the
969 lattice plane (200) of Mnt. **(d)** the enlarge of marked area "d" in **a**. **(e)** FFT pattern of

970 **d**, revealing that Mgh particle is along the zone axis [$1\bar{6}9$] and the lattice of Mnt with
971 (200). **(f)** FFT pattern with the specific spots being removed. **(g)** IFFT image generated
972 from **g**, showing obvious lattice fringes belonging to the ($\bar{3}2\bar{1}$) and ($\bar{3}11$) plane of Mgh.
973 **(h)** FFT pattern of the marked area "i" in **a**, showing the Mgh along the zone axis [$\bar{1}3\bar{3}$].
974 **(i)** FFT pattern of the marked area of "h" in **a**, showing the Hem along zone axis [$0\bar{9}3$].

975 **Figure 8.** Analysis of the transformation degree in different regions of Fh2/Mnt1-600-
976 1. **(a)** TEM image. The insets in **a** represent EDS mappings of Fe and Si. **(b and c)** The
977 HRTEM images of the corresponding area in **a**. The insets in **b** and **c** are the
978 corresponding FFT pattern. **(d-f)** SAED of the selected area in **a** with different ratios of
979 Fe/Si.

980 **Figure 9.** Schematic for the nonaqueous transformation of Fh in different systems. **(a)**
981 The nonaqueous transformation of pure Fh. **(b)** The retarded and heterogeneous
982 transformation of Fh in heteroaggregates. **(c)** The characteristics of surface interactions
983 between Fh and Mnt. The heteroaggregates show the heterogeneous transformation of
984 Fh by changing the strength of interactions and heating conditions: ① low
985 transformation degree of Fh and formation of Hem and Mgh in the heteroaggregates
986 caused by strong interactions between Fh and Mnt, relatively low heating temperature,
987 and/or short heating duration; ② further transformation of the iron (oxyhydr)oxides
988 to Hem with increasing heating temperature and/or duration; ③ high transformation
989 degree of Fh and formation of Hem in the heteroaggregates caused by weak interactions

990 between Fh and Mnt, high heating temperature, and/or long heating duration.

Figure 1

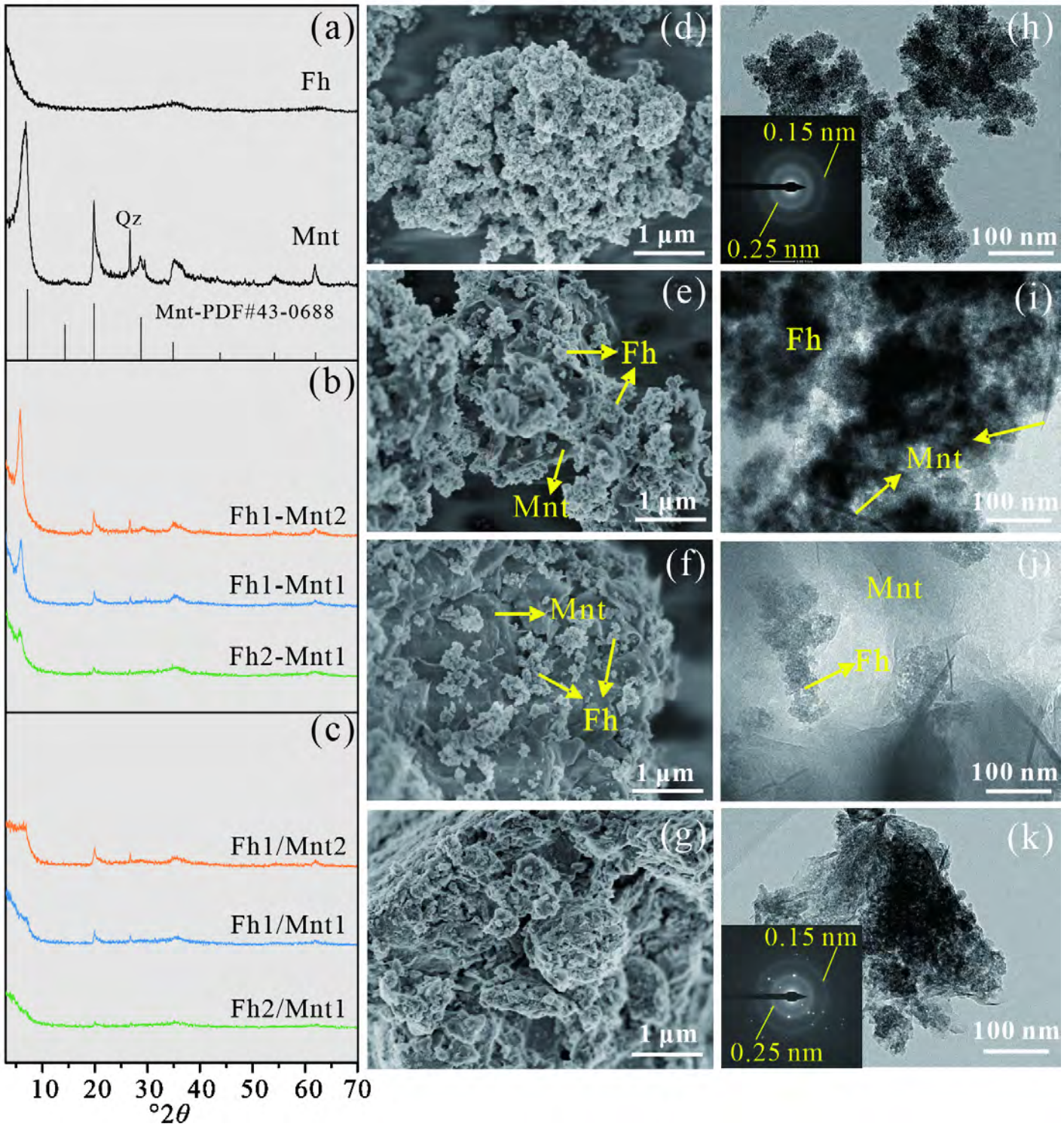

This is the peer-reviewed, final accepted version for American Mineralogist, published by the Mineralogical Society of America.
The published version is subject to change. Cite as Authors (Year) Title. American Mineralogist, in press.
DOI: https://doi.org/10.2138/am-2022-8520. http://www.minsocam.org/

Figure 2

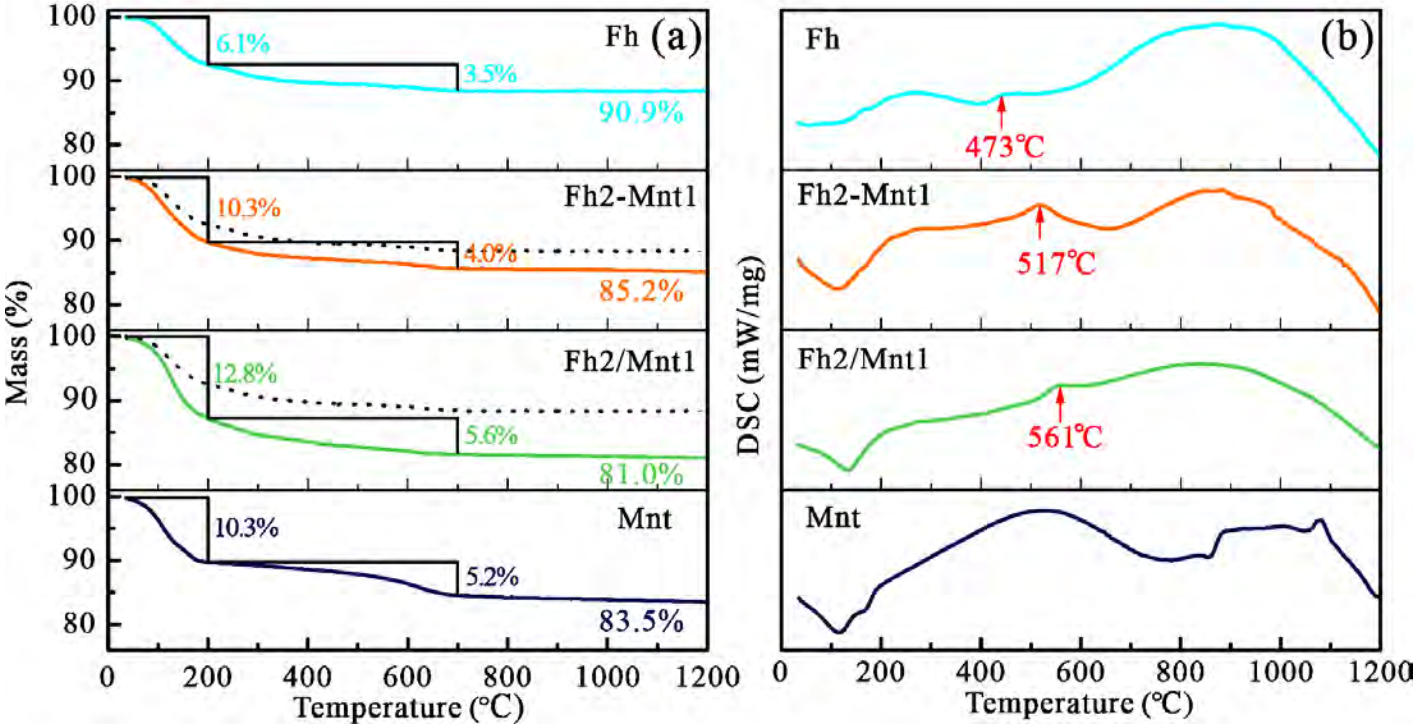

This is the peer-reviewed, final accepted version for American Mineralogist, published by the Mineralogical Society of America.
The published version is subject to change. Cite as Authors (Year) Title. American Mineralogist, in press.
DOI: https://doi.org/10.2138/am-2022-8520. http://www.minsocam.org/

Figure 3

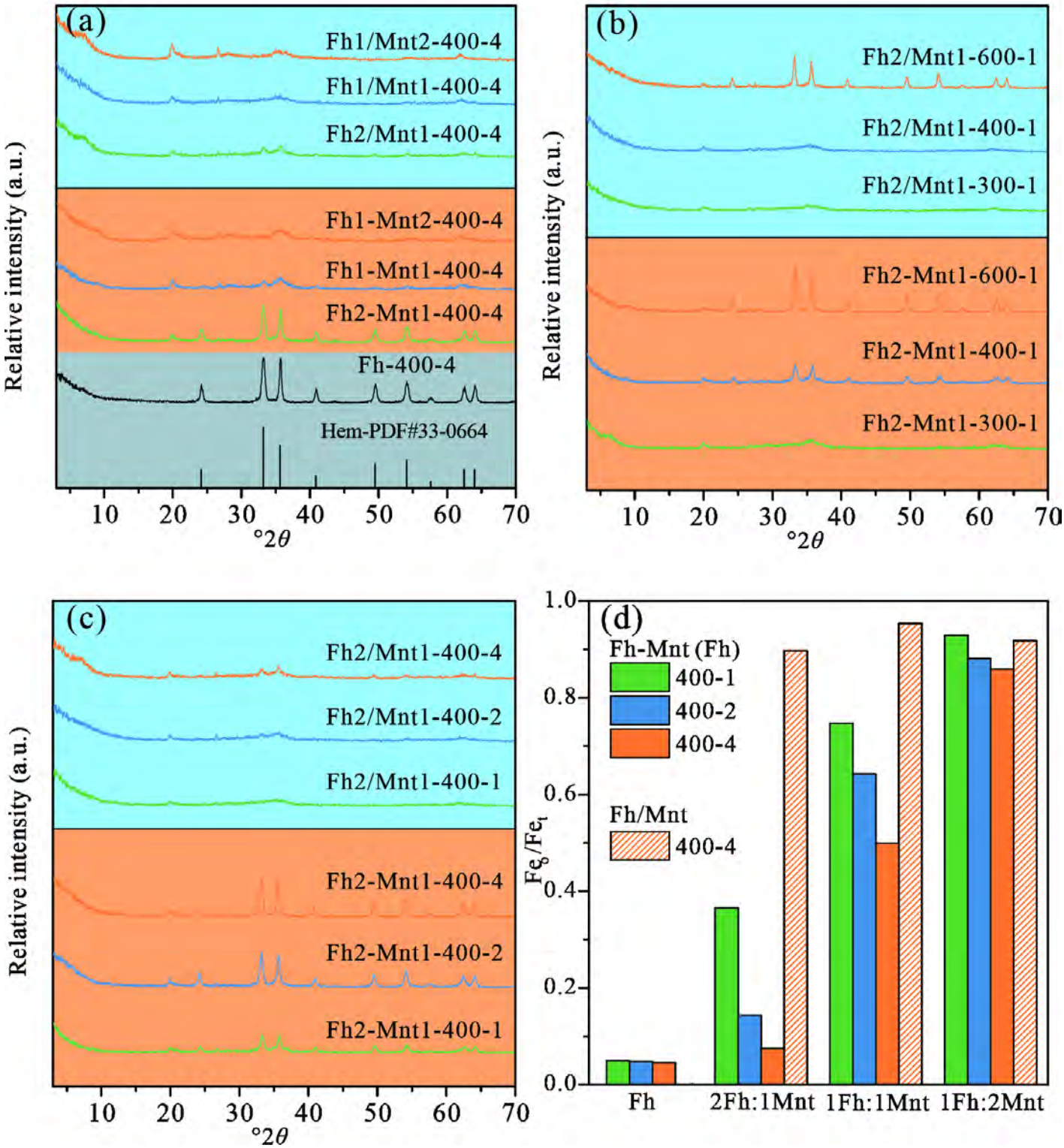

This is the peer-reviewed, final accepted version for American Mineralogist, published by the Mineralogical Society of America.
The published version is subject to change. Cite as Authors (Year) Title. American Mineralogist, in press.
DOI: https://doi.org/10.2138/am-2022-8520. http://www.minsocam.org/

Figure 4

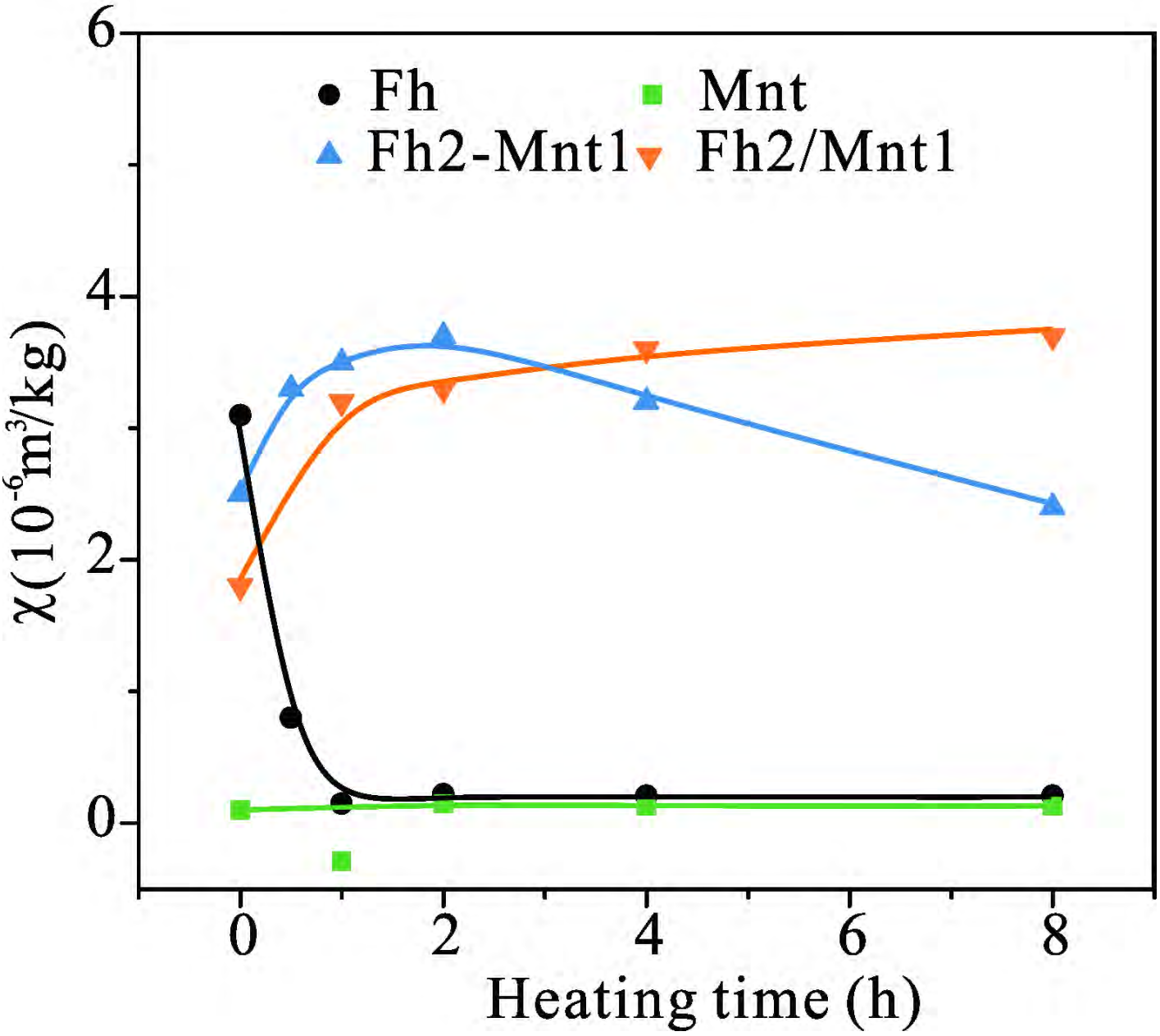

This is the peer-reviewed, final accepted version for American Mineralogist, published by the Mineralogical Society of America.
The published version is subject to change. Cite as Authors (Year) Title. American Mineralogist, in press.
DOI: https://doi.org/10.2138/am-2022-8520. http://www.minsocam.org/

Figure 5

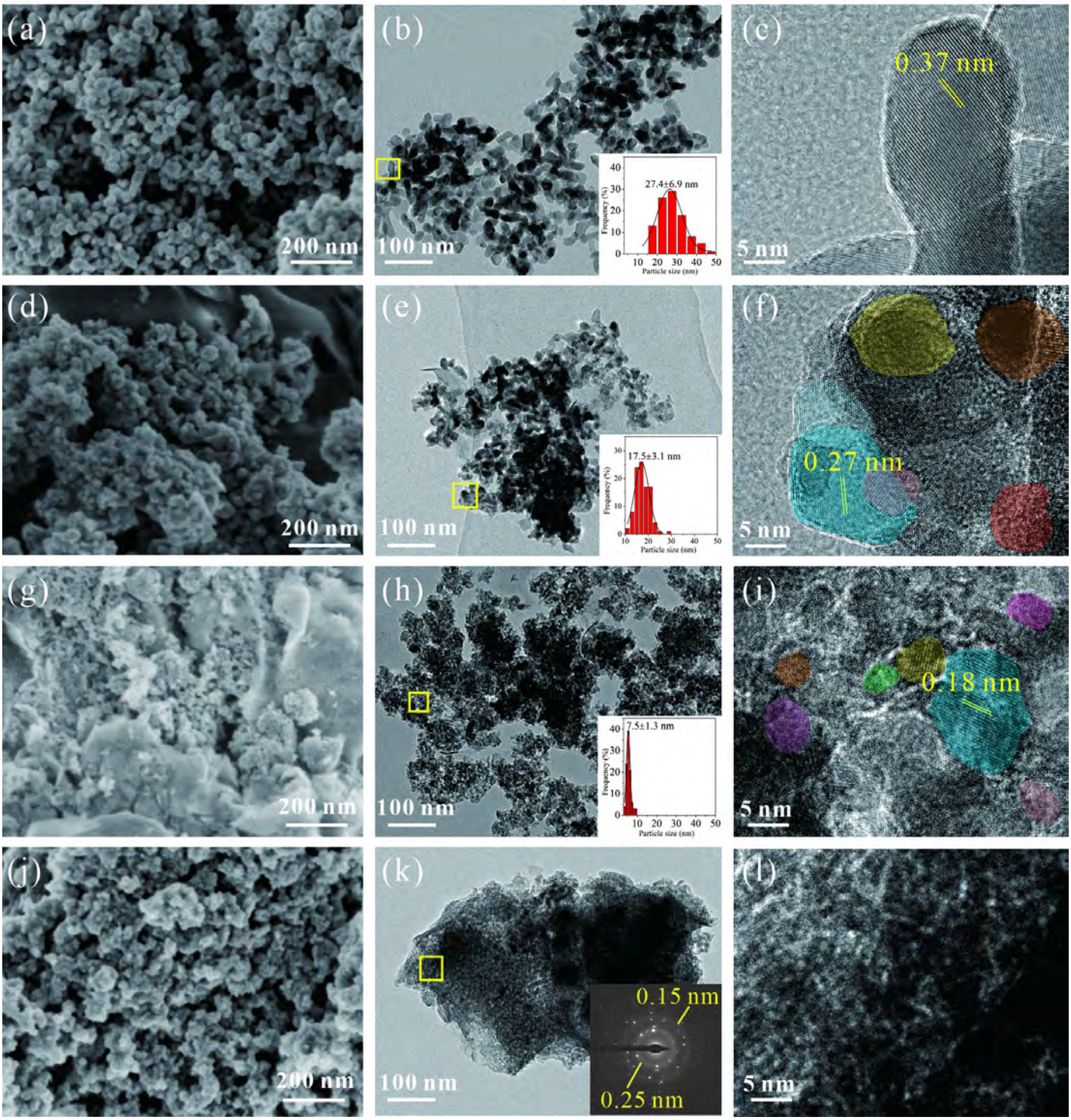

This is the peer-reviewed, final accepted version for American Mineralogist, published by the Mineralogical Society of America.
The published version is subject to change. Cite as Authors (Year) Title. American Mineralogist, in press.
DOI: https://doi.org/10.2138/am-2022-8520. http://www.minsocam.org/

Figure 6

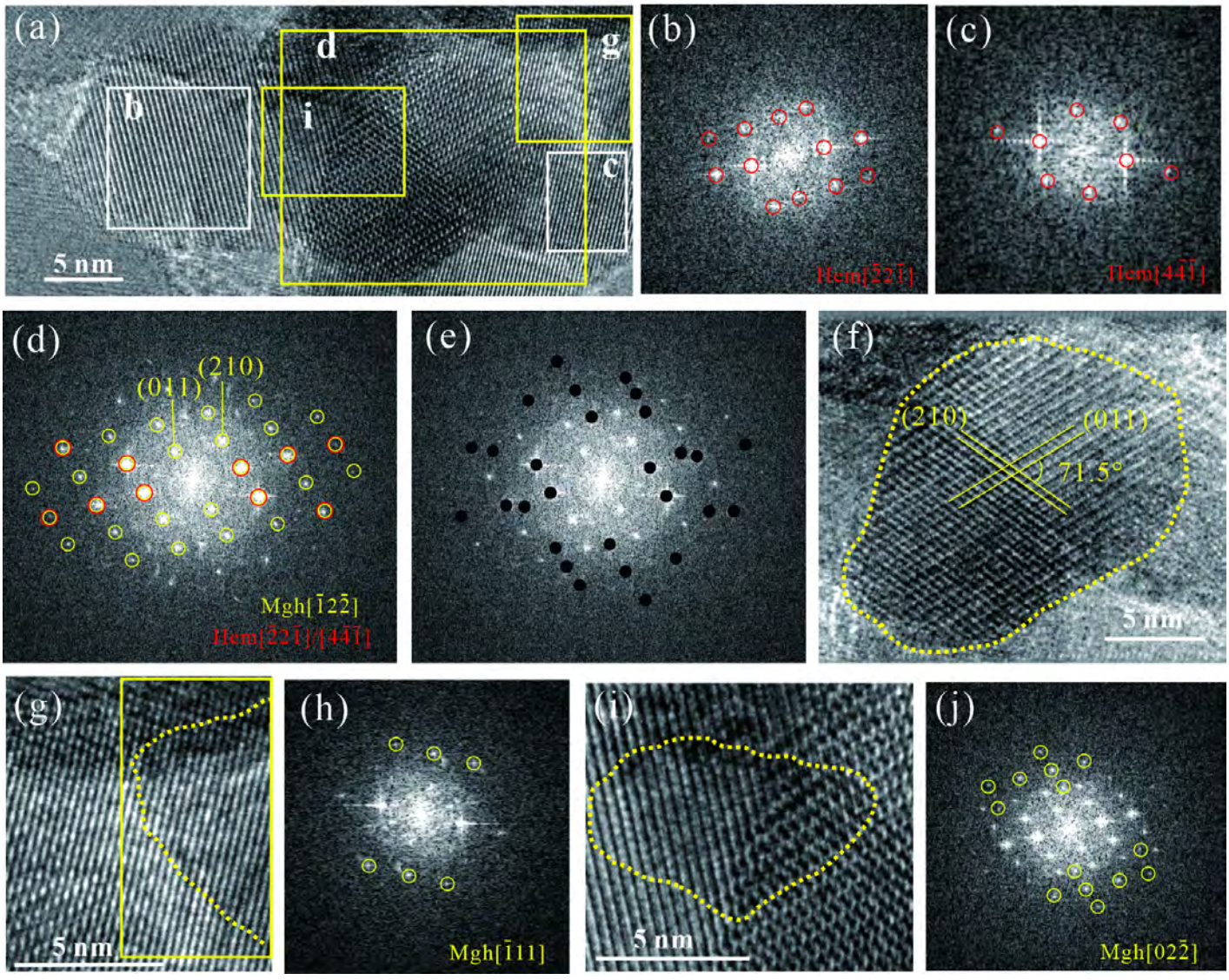

This is the peer-reviewed, final accepted version for American Mineralogist, published by the Mineralogical Society of America.
The published version is subject to change. Cite as Authors (Year) Title. American Mineralogist, in press.
DOI: https://doi.org/10.2138/am-2022-8520. http://www.minsocam.org/

Figure 7

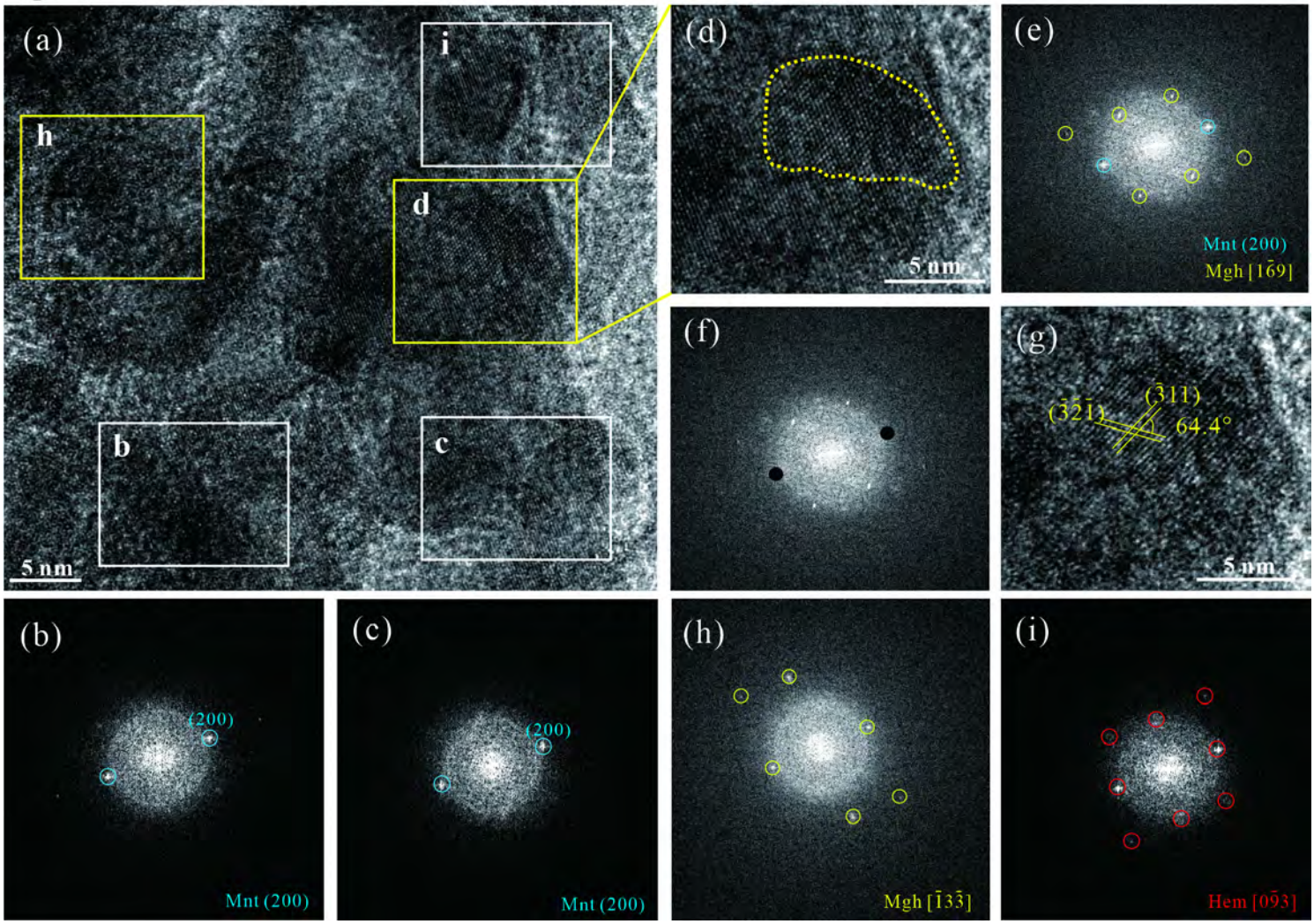

This is the peer-reviewed, final accepted version for American Mineralogist, published by the Mineralogical Society of America.
The published version is subject to change. Cite as Authors (Year) Title. American Mineralogist, in press.
DOI: https://doi.org/10.2138/am-2022-8520. http://www.minsocam.org/

Figure 8

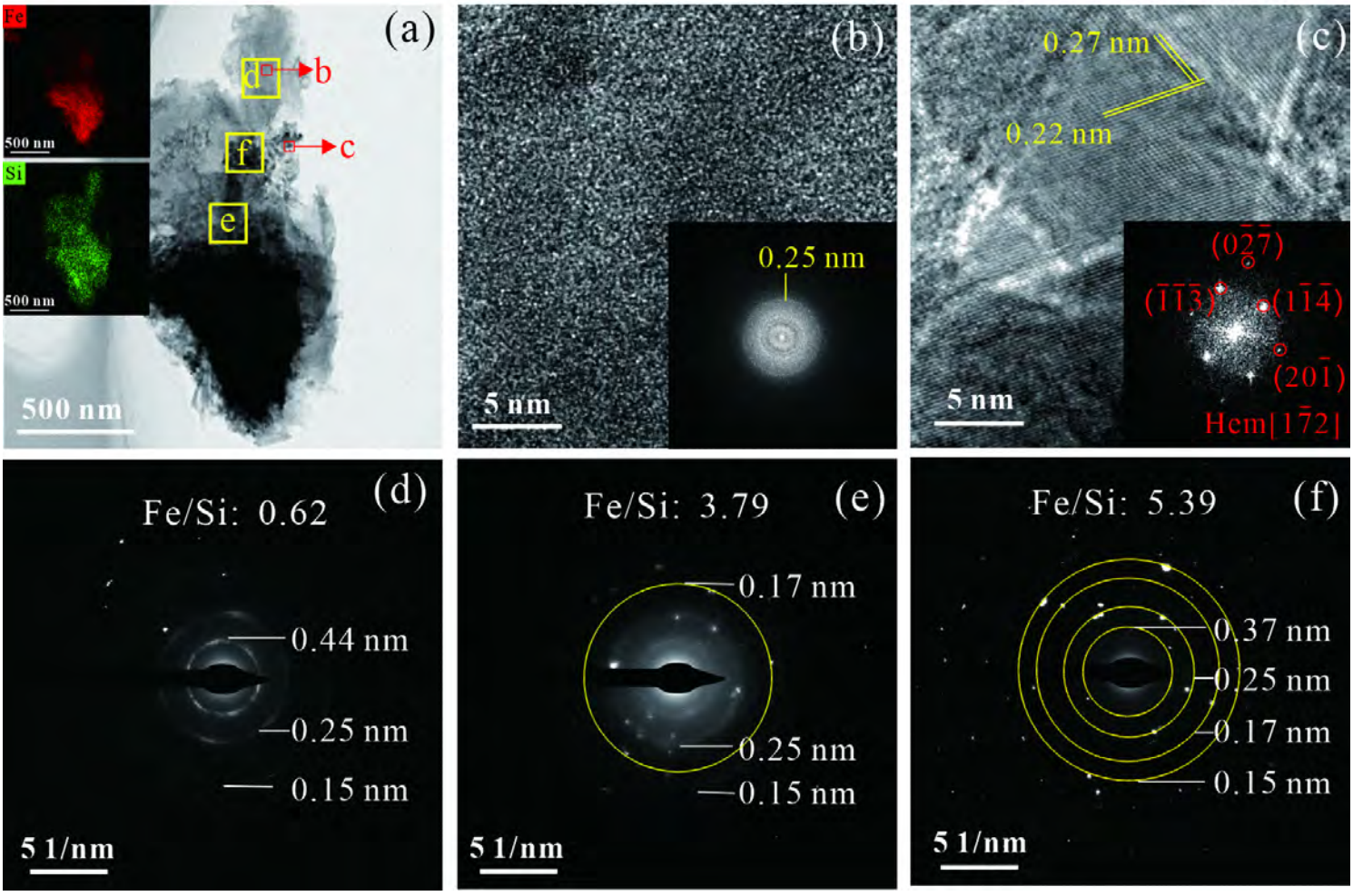

This is the peer-reviewed, final accepted version for American Mineralogist, published by the Mineralogical Society of America.
The published version is subject to change. Cite as Authors (Year) Title. American Mineralogist, in press.
DOI: https://doi.org/10.2138/am-2022-8520. http://www.minsocam.org/

Figure 9